Available online at www.sciencedirect.com
ScienceDirect
Geochimica et Cosmochimica Acta xxx (2007) xxx–xxx
Geochimica
www.elsevier.com/locate/gca

Crystal–melt partitioning of noble gases (helium, neon, argon, krypton, and xenon) for olivine and clinopyroxene

Veronika S. Heber [a,*], Richard A. Brooker [b,1], Simon P. Kelley [a], Bernard J. Wood [b,2]

[a] Department of Earth Sciences, The Open University, Walton Hall, Milton Keynes MK7 6AA, UK
[b] Department of Earth Sciences, University of Bristol, Wills Memorial Building, Queens Road, Bristol BS8 1RJ, UK

Received 24 February 2006; accepted in revised form 1 November 2006

Abstract

Mineral–melt partition coefficients of all noble gases ($^{min/melt}D_i$) have been obtained for olivine (ol) and clinopyroxene (cpx) by UV laser ablation (213 nm) of individual crystals grown from melts at 0.1 GPa mixed noble gas pressure. Experimental techniques were developed to grow crystals virtually free of melt and fluid inclusions since both have been found to cause profound problems in previous work. This is a particularly important issue for the analysis of noble gases in crystals that have very low partition coefficients relative to coexisting melt and fluid phases. The preferred partitioning values obtained for the ol–melt system for He, Ne, Ar, Kr, and Xe are 0.00017(13), 0.00007(7), 0.0011(6), 0.00026(16), and $0.0006^{(+9)}_{(-6)}$, respectively. The respective cpx–melt partition coefficients are 0.0002(2), 0.00041(35), 0.0011(7), 0.0002(2), and $0.0002^{(+3)}_{(-2)}$. The data confirm the incompatible behaviour of noble gases for both olivine and clinopyroxene but unlike other trace elements these values show little variation for a wide range of atomic radius. The lack of dependence of partitioning on atomic radius is, however, consistent with the partitioning behaviour of other trace elements which have been found to exhibit progressively lower dependence of $^{min/melt}D_i$ on radius as the charge decreases. As all noble gases appear to exhibit similar $^{min/melt}D_i$ values we deduce that noble gases are not significantly fractionated from each other by olivine and clinopyroxene during melting and fractional crystallisation. Although incompatible, the partitioning values for noble gases also suggest that significant amounts of primordial noble gases may well have been retained in the mantle despite intensive melting processes. The implication of our data is that high primordial/radiogenic noble gas ratios (^{3}He/^{4}He, ^{22}Ne/^{21}Ne, and ^{36}Ar/^{40}Ar) characteristic of plume basalt sources can be achieved by recycling a previously melted (depleted) mantle source rather than reflecting an isolated, non-degassed primordial mantle region.

1. Introduction

Noble gases are among the most important trace elements used by Earth scientists as tools for investigating the geochemical evolution of the earth. Their inertness, their scarcity, and the combination of both radiogenic or nucleogenic, respectively (^{4}He, ^{21}Ne from ^{235,238}U, ^{232}Th; ^{40}Ar from ^{40}K and ^{129}Xe from ^{129}I) and non-radiogenic (primordial, e.g., ^{3}He and ^{36}Ar) isotopes make noble gases ideal tracers for quantifying geochemical and geodynamical processes in the mantle, the crust, and the atmosphere (e.g., Porcelli and Wasserburg, 1995; Farley and Neroda, 1998; Kamijo et al., 1998; Ozima and Igarashi, 2000; Porcelli et al., 2001; van Keken et al., 2002; Ballentine et al., 2003). Noble gases are central in a vivid debate concerning the mode(s) of mantle convection over geological timescales.

Noble gas isotopic ratios of mantle-derived materials show systematic variations that support large-scale mantle

* Corresponding author. Present address: Institute for Isotope Geology and Mineral Resources, ETH Zürich, 8092 Zürich, Switzerland. Fax: +41 44 6321179.
E-mail address: heber@erdw.ethz.ch (V.S. Heber).
[1] Present address: Department of Earth Sciences, University College London, Gower Street, London WC1E 6BT, UK.
[2] Present address: Department of Earth and Planetary Sciences, Macquarie University, NSW 2109, Australia.

0016-7037/$ - see front matter © 2006 Elsevier Inc. All rights reserved.
doi:10.1016/j.gca.2006.11.010

heterogeneities. Indeed, basalts erupted along mid-ocean ridges (MORB) appear to define a limited variation in the isotopic composition of helium. Lavas and fluids associated with mantle plume domains (such as ocean island basalts—OIB) present much more variable $^{3}He/^{4}He$ values and have been interpreted as representing a mantle domain less degassed than the convective mantle feeding mid-ocean ridge magmatism and, because of its association with mantle plumes, located at a greater depth than the MORB source. This view is consistent with geochemical models advocating a convectively layered mantle over much of the Earth's history (e.g., Kaneoka, 1983; O'Nions, 1987; Allègre et al., 1987; Farley and Neroda, 1998; Allègre and Moreira, 2004). However, recent advances in seismic tomography indicate that plates can be subducted well below the 670 km discontinuity down to the core-mantle boundary (e.g., van der Hilst et al., 1997; Bijwaard and Spakman, 1998; Fukao et al., 2001), and numerical modelling of mantle convection patterns (van Keken and Ballentine, 1999) cast doubt upon the likelihood of maintaining a deep region of the mantle isolated over geological timescales. An additional observation challenging the view of a less degassed mantle domain isolated from a degassed upper mantle is that plume-related samples contain generally lower noble gas concentrations than MORB (e.g., Farley and Neroda, 1998; Ozima and Igarashi, 2000).

In order to reconcile these apparently contradictory views, it has been proposed that noble gases might be fractionated from other trace elements during melt extraction from the mantle (e.g., Albarède, 1998; Ballentine et al., 2002; Meibom et al., 2003; Class and Goldstein, 2005). In this way, noble-gas/radioactive isotope ratios (e.g., $^{3}He/(^{235,238}U + {}^{232}Th)$) may fractionate to produce low $^{3}He/^{4}He$ ratios in MORB compared to OIB values when integrated over long times. In this scenario, high $^{3}He/^{4}He$ ratios in plume-related basalts might reflect the influence of a recycled, previously depleted mantle in the source (Graham et al., 1990; Brooker et al., 2003b). A preferential depletion in U and Th compared to the depletion of noble gases would result in relatively unradiogenic He isotopic composition associated with low He abundances observed in OIB.

Available data for noble gas partition coefficients ($^{min/melt}D_i$, expressed as the ratio of weight concentration of a noble gas i in the mineral and in the melt) allow the exploration of these scenarios quantitatively. Estimates based on the analysis of noble gases in coexisting mineral phases and glass of MORB suggested that these elements are very incompatible (Kurz et al., 1982; Marty and Lussiez, 1993; Valbracht et al., 1994), the upper limits for $^{ol/melt}D_{He}$ and $^{ol/melt}D_{Ar}$ measured in natural olivine/basaltic melt being 0.008 and 0.003, respectively (Marty and Lussiez, 1993). In contrast, pioneering experiments to determine noble gas partition coefficients between synthetic mineral phases and silicate melt yielded variable and fractionated $^{min/melt}D_i$ values suggestive of slightly incompatible or even compatible behaviour for all noble gases (Hiyagon and Ozima, 1986; Broadhurst et al., 1992; Shibata et al., 1994). In several of these experiments compatibility was observed to increase with increasing noble gas atomic radii. However, these results are now generally believed to have been affected by experimental artefacts such as adsorption of heavy noble gases on powdered samples, contamination of separated mineral phases by residual glass, and trapping of noble gases in fluid inclusions during mineral growth (Ozima and Podosek, 2002). The development of 'in situ' analysis by UV laser ablation (Kelley et al., 1994) has provided a technique to circumvent many of these problems. This technique was successfully applied to determine partition coefficients of Ne to Xe between clinopyroxene and melt and Ar between olivine and melt (Brooker et al., 1998, 2003a; Chamorro et al., 2002). These studies have suggested low D values between 10^{-4} and 10^{-2} over a range of clinopyroxene compositions, pressure (0.1–8 GPa) and temperature (1200–1665 °C). Recent experiments by Parman et al. (2005) measuring the He solubility in olivines appear to support the incompatible behaviour for He ($^{ol/melt}D_{He}$: 0.0025–0.006).

Here, we report results of new experiments on olivine–silicate melt partitioning of noble gases and provide new gas analyses of the clinopyroxene and glass (RB586) previously analysed by Brooker et al. (2003a) but now including data for He. We present here for the first time a complete data set of olivine–melt ($^{ol/melt}D_i$) and clinopyroxene–melt ($^{cpx/melt}D_i$) partition coefficients for all noble gases obtained by UV laser ablation, and provide noble gas D values for two major crystalline phases of the Earth's mantle that are important to reveal bulk noble gas partitioning coefficients as function of mantle composition. Since the study of Brooker et al. (2003a), we have further developed the UV laser technique by introducing a 213 nm laser equipped with a new optical system leading to a more precise control on ablation, and a detailed characterisation of individual crystals prior to and during analysis. Compared to previous UV laser ablation studies (Brooker et al., 1998, 2003a; Chamorro et al., 2002), this system allows a more rigorous spatial control on the ablated phase, preventing accidental ablation of glass or fluid and melt inclusions. These developments allow us to measure very low He abundances and low partition coefficients that are characteristic of mantle mineral phases. In summary, the partitioning data enable us to characterise the absolute and relative degree of fractionation of light and heavy noble gases (He, Ar, and Xe) as well as their radioactive parents (U, Th, and K).

2. Experimental and analytical techniques

2.1. Starting materials and experimental techniques

General experimental techniques are described here. Details are given in Section 2.1.1 for the olivine (N2SFo) and in Section 2.1.2 for the clinopyroxene ($Di_{60}Ab_{40}$) experiment. A discussion of the approach to reach equilibrium conditions for both crystals and melts is given in Appendix A.1.

Please cite this article in press as: Heber, V.S. et al., Crystal–melt partitioning of noble gases (helium, neon, argon, ..., *Geochim. Cosmochim. Acta* (2007), doi:10.1016/j.gca.2006.11.010

Starting materials for experiments were glasses prepared from reagent grade oxides (SiO_2, MgO, and Al_2O_3) and carbonate ($CaCO_3$, Na_2CO_3) for the clinopyroxene experiment (RB586, RB585) or spec-pure grade for three olivine experiments (RB587, RB588, and RB589). These mixtures were decarbonated and then melted in a vertical tube furnace. Starting materials have a nominal composition of 60:40 mol% diopside: albite ($Di_{60}Ab_{40}$) for the clinopyroxene experiment and 66.6:33.3 mol% sodium disilicate ($Na_2Si_2O_5$): forsterite (Mg_2SiO_4) (N2SFo) for the three olivine experiments. The $Di_{60}Ab_{40}$ glass was doped with a cocktail of trace elements in order to compare the experiments with earlier work on trace element partitioning in olivine and clinopyroxene, then remelted and reground through a number of cycles. Further, the spec-pure N2SFo glass was split into three aliquots, RB588 was doped with 200 ppm Sc, RB589 with 200 ppm Ti and RB587 left undoped. Sc and Ti were added to investigate the possibility that a charge-balancing cation mechanism could have a significant effect on the partitioning values (see Brooker et al., 2003a). Major and trace elements measured by electron microprobe analysis (EMPA) for the $Di_{60}Ab_{40}$ starting material (RB585) and the N2SFo run products after ~10% crystallisation are presented in Table 1. The trace element partition coefficients of RB586 were reported by Brooker et al. (2003a).

Starting materials were loaded into platinum capsules that were left open to the noble gas pressure medium. Crystals were grown by cooling slowly from above the liquidus in a high-pressure noble gas atmosphere using a TZM (titanium–zirconium–molybdenum) rapid quench cold-seal vessel (University of Bristol). Temperature was controlled using a Eurotherm programmable controller. The measured composition of the gas phase was 24.6–23.2–25.0–22.2–5.0 mol% for He–Ne–Ar–Kr–Xe, respectively. At the end of the experiments the samples were quenched (>200 °C/s) by rapidly lowering the sample into the water-cooled section of the vessel using an external magnet.

Selected fragments of quenched samples containing both crystal and melt phases were mounted in dental resin and ~0.5 mm thick doubly polished sections were prepared (Brooker et al., 1998). Thus, we avoided the standard practice of using heated glue to mount/demount sections on glass sides. As will be shown below heating would have caused significant diffusive He loss from the glass phase. As a consequence, all preparation techniques were undertaken at room temperature. Several fragments were selected from a given experiment, each containing reasonably-sized crystals (~100 μm) for laser ablation. The samples were ultrasonically cleaned in acetone, methanol and finally deionised water.

As with other attempts to experimentally determine noble gas $^{min/melt}D_i$ (Hiyagon and Ozima, 1986; Brooker et al., 1998; Chamorro et al., 2002), there are several challenges that needed to be overcome in order to achieve reproducible results. In particular, the presence of fluid and/or melt inclusions was a major problem for analysis, whether in the crystals (see below), or in the melt where larger bubbles leaked He and Ne continuously into the vacuum system. It was also necessary to test for adsorption and absorption on mineral surfaces that could have lead to enhanced $^{min/melt}D_i$ values. Finally, the size and shape of crystals is critical for the laser ablation technique. On the one hand crystals need to be large enough to allow ablation of volumes that release measurable amounts of gas, while on the other they have to be grown sufficiently slowly to remain in equilibrium with the melt. As a result, a number of experimental protocols were developed to improve the accuracy of the experimental data.

2.1.1. N2SFo experiments

The sodium disilicate–forsterite system (N2SFo) was selected for the olivine growth experiment because alkali-rich melts tend to have very low viscosities (Dingwell et al., 1998) allowing bubbles to escape more easily than from melts of high viscosity. Furthermore, the liquidus temperature for the selected starting composition is low (approximately 1035 °C, and thus comfortably below the limit of the operating range of the TZM vessel). This material was loaded as a powder (grain size <25 μm) and melted in a noble gas atmosphere of ~101 MPa. This procedure has the advantage that the noble gas pressure medium is distributed throughout the sample as it melts, reducing the time required for equilibration of the melt. Since for analyses of noble gases bubbles are problematic, we developed a method which we found minimised the bubble content of the melt and the coexisting olivine crystals. Glasses quenched from melts that had been held for 5 h above the liquidus did not contain any bubbles. However, as samples were cooled below the liquidus at constant pressure, bubbles developed within or on the surface of the growing crystals as shown in Fig. 1 for an earlier sample (RB571, not considered in this study), even though the rest of the glass appeared to be bubble-free. RB571 was held above the liquidus for 7 h, then cooled isobarically from

Table 1
Electron microprobe analyses of starting materials and run products

	Starting mix		Run products							
	$Di_{60}Ab_{40}$	N2SFo[a]	RB586		RB587		RB588		RB589	
			Glass	Cpx	Glass	Olivine	Glass	Olivine	Glass	Olivine
No. of analyses	*30*		*7*	*12*	*7*	*8*	*16*	*9*	*14*	*4*
wt%										
SiO_2	63.9(6)	59.50	64.6(7)	55.0(5)	61.2(6)	42.6(4)	60.5(7)	42.9(1.4)	57.7(8)	42.8(1.5)
Al_2O_3	11.5(1)		13.5(4)	0.91(13)	n.a.	n.a.	n.a.	n.a.	n.a.	n.a.
FeO	b.d.		n.a.	n.a.	b.d.	b.d.	b.d.	b.d.	b.d.	b.d.
MgO	6.7(2)	15.95	4.45(4)	19.2(3)	14.6(2)	56.7(2)	15.5(1)	57.0(7)	15.6(2)	55.5(1.4)
CaO	10.4(3)		8.3(3)	24.9(3)	n.a.	n.a.	n.a.	n.a.	n.a.	n.a.
Na_2O	7.1(1)	24.50	8.1(3)	0.36(6)	23.4(2)	0.008(5)	24.3(2)	0.027(11)	23.3(3)	0.003(3)
K_2O	0.06(1)		b.d.	b.d.	n.a.	n.a.	n.a.	n.a.	n.a.	n.a.
Total	99.64		99.66	100.31	99.18	99.33	100.37	100.11	96.61	98.3
ppm										
Sc	n.a.		b.d.	b.d.	n.a.	n.a.	234(35)	624(243)	n.a.	n.a.
Ti	n.a.		b.d.	b.d.	b.d.	b.d.	n.a.	n.a.	199(71)	30(35)

Numbers in parentheses given here and in following tables represent $1-\sigma$ uncertainties in units of the least significant digit. Starting material ($Di_{60}An_{40}$) and run products (N2SFo) were analysed using Cameca SX100 at Open University. Composition of RB586 run products from Brooker et al. (2003a).
Glass analyses: 20 keV, 20 nA, beam size 30 μm, 5 s on each Na, Mg, Si; 15 s on Ti or Sc and Fe.
Crystal analyses: 20 keV, 20 nA, beam size 10 μm, 10 s on each Na, Mg, Si; 30 s on Ti or Sc and Fe.
n.a., not analysed; b.d., below detection.
[a] Nominal composition.

Please cite this article in press as: Heber, V.S. et al., Crystal–melt partitioning of noble gases (helium, neon, argon, ..., *Geochim. Cosmochim. Acta* (2007), doi:10.1016/j.gca.2006.11.010

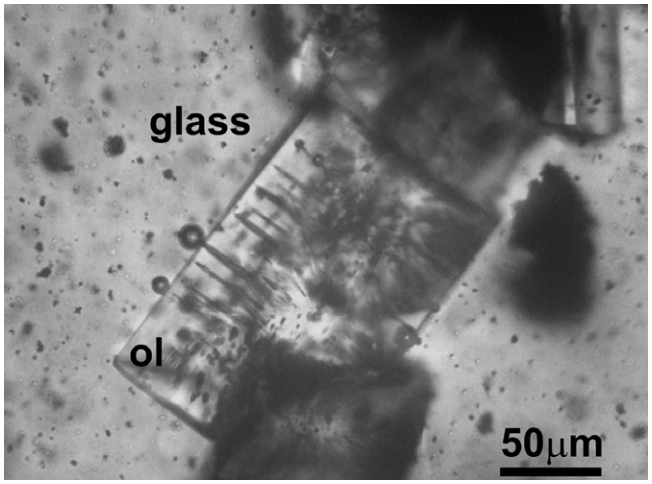

Fig. 1. Optical microscope image of RB571. Bubbles seen around the olivine (ol) edge with trails extending into the crystal interior. A comparison with Fig. 3 shows the success of the different experimental approach for the RB587–589 samples in producing bubble-free olivine crystals.

1040 to 1005 °C at 0.6 °C/h. Such a temperature decrease might have reduced the solubility of noble gases in the melt, resulting in preferential bubble nucleation along the mineral surfaces. Many bubbles were observed around the edges of crystals with trails extending into the crystal interior (Fig. 1), suggesting that the bubbles were formed during an early stage of growth. To minimise bubble growth subsequent experiments employed an increase of pressure by 10% at the initial stages of crystal growth. This significantly reduced bubble formation (see Figs. 2 and 3). The RB587–589 samples were run together and held at 1165 °C for 1 h then cooled over 3 h to 1045 °C, while maintaining the gas pressure of ~101 MPa. The pressure was then increased to 111.2 MPa and the samples cooled at 0.6 °C/h to 990 °C ensuring that the pressure was not allowed to drop below 109 MPa. Finally, the samples were left at these conditions for 6 h. This process produced very equant crystals almost free of melt or fluid inclusions (Figs. 2 and 3). Occasional gas bubbles identified in the olivine crystals were generally around 5 μm in diameter, but we cannot exclude the possibility that smaller, sub-microscopic bubbles existed.

2.1.2. $Di_{60}Ab_{40}$ experiments

Pilot clinopyroxene growth experiments were undertaken using powdered glass as starting material, which was loaded into the Pt capsule and melted at pressure to introduce noble gases into the resulting liquid. At the chosen run conditions, the quenched glasses always contained bubbles ranging in size from <5 to 200 μm. It may be that such bubbles were retained from the initial voids in the starting powder and were captured during crystal growth. The concentration of bubbles was greater if samples were taken directly to the final temperature rather than cooled from above the liquidus, and in addition, the crystals were smaller or non-euhedral in the former cases. To counteract the bubble problem, the glass powder was loaded into the capsule and heated to 1530 °C, above the liquidus in a 1 atm tube furnace (i.e., in air) for 1 h. This procedure removed nearly all bubbles due to the low viscosity (and/or low gas pressure). The melt was quenched to a glass and retained in the capsule. Two samples prepared this way were then loaded into the TZM vessel and subjected to a noble gas pressure of 102 MPa at a super-liquidus temperature of 1285 °C. The capsules of RB585 and RB586 were 12 and 3 mm long, respectively (the length of RB585 was intended as a diffusion test). A time of 9 h was allowed for the noble gases to diffuse into the melt from the surface. The experiment was quenched at this point and RB585 was removed to determine noble gas diffusion rates (see Appendix A.1). The sample RB586 was then reloaded into the TZM vessel and taken back to 1290 °C at a slightly higher gas pressure of 112 (±1) MPa for the crystal growth experiment. Although this requires a slight re-equilibration for the fluid, it assures that any remaining bubbles dissolve and any bubble nucleation or growth during the initial cooling stage is inhibited. RB586 was heated to 1290 °C for 30 min, then cooled in a series of steps to 1272 °C (still above the liquidus) over a 1 h period. The temperature was then decreased at a rate of 1.2 °C/h to the approximate liquidus temperature of 1260 °C, and subsequently cooled from 1260 to 1200 °C at a cooling rate of 0.6 °C/h to grow the crystals. The melt was held at these final conditions for 6 h. Crystals grown by this method were generally bubble-free (Fig. 2B).

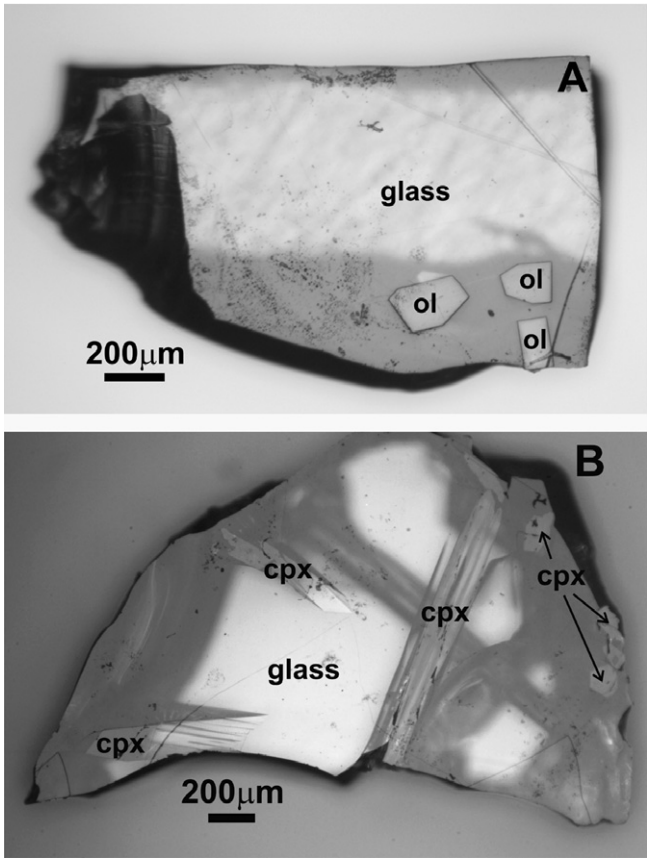

Fig. 2. Optical microscope image in reflected light of RB588A (A) and RB586A (B), showing the different morphologies of the olivine (ol) and the clinopyroxene (cpx) crystals.

2.2. Noble gas analyses and data processing

All UV laser ablation analyses were carried out at the Open University. The NewWave UP213 combined laser/microscope system uses a pulsed quintupled Nd:Yag laser ($\lambda = 213$ nm) with a pulse duration of 4 ns, a repetition rate of 10 Hz, and rastering velocity of 10 or 20 μm/s. The laser energy used in these experiments depended upon the analysed material and varied between 3 J/cm^2 for glass and 10–15 J/cm^2 for crystals. A laser beam of 8 μm in diameter was used to produce precisely targeted, rectangular raster areas, about 5 μm deep, that were positioned in regions devoid of fluid and melt inclusions (Fig. 3C). The duration of laser ablation varied depending on the area of a raster (ranging from 1500 up to about 4000 μm^2) and depth from 6 min for glass to 3–10 min for crystals. Further details regarding the UV laser technique can be found in Kelley et al. (1994).

The extracted gas was cleaned using three SAES AP-10 getters to remove active gases before analysing noble gases with a MAP 215-50 noble gas mass spectrometer. Noble gas isotopes ^{4}He, ^{22}Ne, ^{40}Ar, ^{84}Kr, ^{132}Xe, as well as $^{44}CO_2$ were analysed in one measurement series using a multiplier collector, as abundances were low and similar for all gases and hence no linearity problems were encountered. Mass 22 was corrected for interfer-

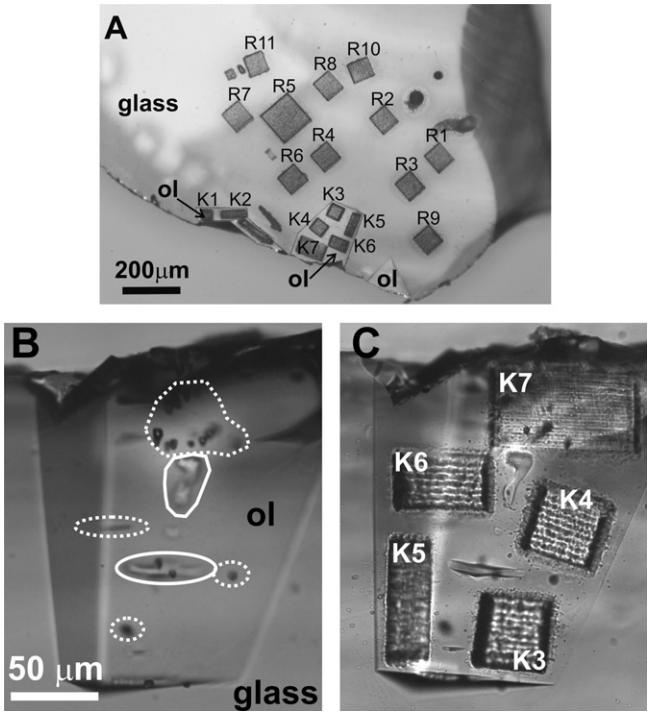

Fig. 3. Optical microscope images of the RB589A experiment. (A) The overview image (reflected light) shows a typical series of laser ablation pits. R1 to R11 and K1 to K7 are laser pits probing the glass and the olivines (ol), respectively. The edges of the crystals are highlighted. (B and C) Enlarged transmitted light microscope images of one olivine crystal. In (B), gas bubbles (black dots, framed by dotted lines) and melt inclusions (framed by solid lines) are shown. (C) The crystal after UV laser ablation, illustrating the ability of the UV laser to avoid inclusions during ablation. Pit K7 was intentionally ablated in an area with bubbles.

ence with $^{44}CO_2^{2+}$ using a pre-determined CO_2^{2+}/CO_2^{+} ratio of 0.010 ± 0.004. The sensitivity of the mass spectrometer was calibrated using an accurately known gas volume from a calibrated gas reservoir and pipette. All noble gases in the calibration reservoir have atmospheric isotopic compositions, but non-atmospheric elemental abundances. The measured amounts of noble gas delivered in the calibration pipette were, in cm^3 STP, 3.72×10^{-9} ^{4}He; 3.25×10^{-10} ^{22}Ne; 3.76×10^{-9} ^{40}Ar; 1.91×10^{-9} ^{84}Kr; and 2.03×10^{-10} ^{132}Xe, calibrated against standards of the Noble Gas Laboratory at ETH Zurich, Switzerland (Heber, 2002).

First, noble gases were analysed in the glass fraction of the respective sample by ablating laser pits away from the crystals. Subsequently, but prior to analysis of the crystals the sample was heated *in vacuo* (170–200 °C for 14–70 h, depending on the size and thickness of the sample) to release He from the glass fraction. This was necessary to minimise the background contribution of He during crystal analysis. The main blank contribution during He analysis was the result of diffusive loss of this element from the glass. Previous diffusion experiments (Trull and Kurz, 1993; Heber et al., 2004) demonstrate that such a heating protocol did not cause significant He loss from olivine and clinopyroxene, because the He diffusion rates in these crystals are many orders of magnitude slower than in the glass. This procedure reduced He blank contributions to a level which allowed analysis of the crystals. It also promoted degassing of adsorbed atmospheric noble gases (mainly Ar).

The noble gas content of the glass of each sample was determined by measuring gases extracted from ~10 pits, each having dimensions of about $60 \times 60 \times 4$ μm (Fig. 3A). We also performed at least one depth profile of about $100 \times 100 \times 7$ μm to monitor diffusive loss of noble gases from the glass during or after sample preparation. The depth profiles show that helium is depleted in the uppermost several micrometres of all samples consistent with diffusion as the controlling loss mechanism (see Appendix A.2, Fig. A.1). We calculated the original He concentration in all glasses, using a ^{4}He/^{22}Ne ratio obtained from analyses well below the surface in samples polished shortly before analysis (RB587F, RB586AII). Details of He and Ne diffusion in glass as well as of the applied correction are given in Appendix A.2.

Noble gases were extracted from the mineral phases by ablating 6–11 raster areas per sample (Table 2). Their sizes were controlled by the sizes and thicknesses of the analysed minerals as well as by the occurrence and distribution of fluid or melt inclusions (cf. Fig. 3C). The areas of the rasters in crystals varied from 1500 to 3800 μm^2 and their depths reached up to 5 μm. Generally, ablated crystal pit volumes are slightly larger or smaller compared to ablated glass volumes, with exception of two samples, which contained only small crystals, that have a crystal to glass pit volume of ~32% (Table 2). The ablation depth is five to 10 times shallower than in previous studies (Brooker et al., 1998, 2003a; Chamorro et al., 2002) improving discrimination against inclusions and increasing the accuracy of the determination of the noble gas crystal and the melt solubilities, despite the fact that gas amounts measured were extremely low.

All noble gas data were corrected for the procedural blank. For glass analyses, before sample heating, blanks were regularly measured and average blank values of ^{4}He, ^{22}Ne, ^{40}Ar, ^{84}Kr, and ^{132}Xe were (in 10^{-12} cm^3 STP) 500–900, 0.6, 14, 0.02, and 0.008, respectively. After heating, the average procedural blanks for ^{4}He, ^{22}Ne, ^{40}Ar, ^{84}Kr, and ^{132}Xe were (in 10^{-12} cm^3 STP) 40–100, 0.2, 7, 0.02, and 0.008, respectively. Since they are more critical, blanks were measured before and after each crystal analysis. To convert measured noble gas abundances into concentrations, the volumes of all laser pits were precisely determined using a non-contact, vertical scanning white light interferometer (Zygo Instrument, Imperial College, London), with nanometre-scale vertical precision (R. Chater, personal communication, 2004). Glass densities calculated using the data from Lange and Carmichael (1987) are 2.44 g/cm^3 for the N2SFo and 2.45 g/cm^3 for the $Di_{60}Ab_{40}$ experiment. The densities of forsterite and diopside are 3.2 g/cm^3 (Deer et al., 1992).

Errors quoted for the noble gas concentrations (Table A.2) are reported as $1-\sigma$ statistical error of the analyses (generally $\leqslant$1% for glass analyses, but they can be as high as 100% for the low concentrations measured in crystals) and include uncertainties resulting from blank and interference (^{22}Ne) corrections. The main source of error results from blank correction of crystal data because of the very low gas abundances in crystals. Negative values in Table A.2 indicate that blank levels were above the nominal gas amounts for corresponding sample. Uncertainties derived from the volume determination (~10%), the elemental composition of the calibration gas (0.5% He, Ne; 1% Ar; 4% Kr, Xe; (Heber, 2002)) and density estimates for the glasses (10%) are not included in the stated errors. The error given for the average noble gas $^{\text{min/melt}}D_i$ for each sample is, unless otherwise stated, the standard deviation of the respective individual $^{\text{min/melt}}D_i$ (Table 3 and footnotes therein). The standard deviation for some average D-values (mainly for Ne, Xe) is larger than 100% and this uncertainty would lead to D-values ranging to physically impossible negative values. This is partly due to the small numbers of samples involved in the calculation (RB587F). Those uncertainties are given as the deviation of the mean and are marked in Table 3 as cursively written numbers or are quoted as upper and lower limit for few average D-values (mostly Xe). These high uncertainties result from the variability of the single values caused by measurements of very low gas abundances in the crystals that were close to blank levels or near the detection limit of the mass spectrometer. The errors given for the average noble gas solubilities in N2SFo and $Di_{60}An_{40}$ glasses in Table 4 are calculated as the standard error of the mean.

3. Results

3.1. Experimental results

Fig. 2A shows the typical appearance of run products of the olivine experiments (RB588A). Forsterite is the only

Table 2
Summary of samples, the quantity of crystals they contained and the quality of crystal analyses

Sample	Crystal phase	Dopant	No. of crystals	Quality of crystals	Number of ablated rasters in crystals			Ratio of average crystal pit volume to glass pit volume (%)
					Total	Pure crystal	Contaminated by glass/bubbles	
RB587B	Olivine	None	4	Very good	8	4	3 / 1	62
RB587F	Olivine	None	>10	Fair (small, many gas bubbles)	10	2	3 / 1	32
							4: too small[a]	
RB588A	Olivine	Sc	3	Very good	7	4	2 / 1	121
RB588B	Olivine	Sc	3	Very good	6	4	0 / 1	96
							1: too small	
RB588C	Olivine	Sc	For depth profile of noble gases in glass (see Appendix A.2)					
RB589A	Olivine	Ti	4	Good (small crystals)	7	3	2 / 1	32
							1: too small	
RB586A	cpx	tr.el.[b]	6	Good (large crystals, but many melt inclusions)	11	5	5 / 0	77
							1: too small	
RB586AII	(Only glass)		Prepared shortly before analysis (for unaltered $^4He/^{22}Ne$ ratio) (see Appendix A.2)					
RB585	(Only glass)		Starting mix for diffusion test					

[a] Means: four raster areas were too small to be further considered.
[b] RB568A was doped with a cocktail of trace elements, see Brooker et al. (2003a).

crystalline phase in these experiments and represents ⩽10% crystallisation, so the melt compositions are close to the bulk compositions. All olivines are euhedral in outline (see also Fig. 3A for RB589A) and almost equal in size, generally 50–150 μm wide and 150–200 μm long. The RB588 series tends to contain the largest crystals. However, in RB587F, the almost euhedral, but slightly smaller olivines grew in radiating aggregates with numerous melt inclusions in the central part. Fig. 2B shows the resulting crystals of the clinopyroxene experiment (RB586A). The crystalline phase is a clinopyroxene with a composition of 94% diopside and minor amounts of jadeite (2%), Ca-Tschermakite (1%) and enstatite (3%) (Brooker et al., 2003a). The amount of clinopyroxene is about 15% in this experiment. The clinopyroxenes are generally euhedral and vary in length from 200 to 1300 μm.

The near perfect euhedral morphology and the rarity of melt inclusions in the olivines suggests a slow and homogenous growth (e.g., Donaldson, 1975). However, a few gas bubbles with diameters of about 5 μm were detected in most of the olivine crystals (Fig. 3B). Also, we observed rare dark spots in the olivines in the range of 400 and 600 nm using an optical microscope with 1000× magnification. These spots could not be further identified, thus representing either bubbles or impurities. However, they are likely to be impurities since examination of all olivine crystals showed that identifiable gas bubbles were all similar in size, all between 4 and 6 μm in diameter without a continuous size distribution down to 600 nm.

The clinopyroxenes usually contained melt inclusions and exhibited melt trapping along very thin planes assumed to be twinning features. In contrast to olivines, no gas bubbles were observed in the clinopyroxenes of RB586A. This lack of bubbles in the clinopyroxenes may be the result of either the different experimental techniques applied to saturate the N2SFo and $Di_{60}Ab_{40}$ starting materials with noble gases (see Section 2.1) or a preference for bubble nucleation on the surface of olivine compared to clinopyroxene.

3.2. Noble gas composition of the glasses and crystals

Noble gas concentrations of glass and crystal analyses are presented in Tables A.2.1–A.2.6 of Appendix A.2. The glass of each sample was analysed using equally sized raster pits distributed throughout the section with at least one depth profile. The noble gases are homogeneously distributed in all N2SFo and the $Di_{60}Ab_{40}$ glasses with variations of ⩽5% for Ne, Ar, and Kr. Variations are somewhat larger for Xe ⩽10% in both glasses (Table A.2). The larger variability of Xe might be either due to the lower Xe content used in the experiment, which makes the measured low Xe concentration prone to contribution of adsorbed Xe, or the lack of diffusional equilibrium (see Appendix A.1). Average noble gas melt solubilities of the N2SFo and the $Di_{60}An_{40}$ compositions are presented in Table 4.

Noble gases concentrations measured in the crystals are given in Table A.2. The quality and the number of crystals

Table 3
Single and average noble gas mineral–melt partitioning coefficients obtained from crystal analyses in this work

Sample	Raster	$^{min/melt}D_{He}$	$^{min/melt}D_{Ne}$	$^{min/melt}D_{Ar}$	$^{min/melt}D_{Kr}$	$^{min/melt}D_{Xe}$
RB587B	Pure olivine analyses					
	K2	0.0002(2)	0.0003(5)	0.003(2)	0.0014(3)	0.009(4)
	K3	neg.	0.0010(2)	0.0019(7)	0.0009(3)	neg.
	K6	0.0006(3)	neg.	0.003(1)	neg.	0.006(4)
	K7	0.0006(3)	0.0005(8)	0.0002(9)	neg.	neg.
Average $^{ol/melt}D_i$		**0.00035***(24)*	**0.00045***(29)*	**0.0020(13)**	**0.00056***(56)*	**0.0039***(39)*
	Crystal analyses compromised by contamination with glass or gas bubbles					
	K1 (g)	0.0016(5)	0.0007(8)	0.010(1)	0.0014(8)	0.009(7)
	k4 (g)	neg.	neg.	0.0115(9)	0.0061(8)	neg.
	K5 (g)	neg.	0.0003(8)	0.005(2)	0.0034(5)	neg.
	K8 (b)	2.8(2)	8.6(6)	a.d.	a.d.	351(62)
RB587F	Pure olivine analyses					
	K4	0.0029(5)	0.0016(6)	0.009(2)	0.0011(3)	0.025(8)
	K9	neg.	0.0003(12)	0.00002(170)	0.0011(7)	neg.
Average $^{ol/melt}D_i$		**0.0014***(14)*	**0.0010***(7)*	**0.0043***(43)*	**0.0011***(0)*	**0.013***(13)*
	Crystal analyses compromised by contamination with glass or gas					
	K1 (g)	0.0007(8)	0.003(2)	0.032(3)	0.024(1)	neg.
	K3 (g)	0.0053(5)	0.0114(7)	0.044(3)	0.036(2)	0.007(7)
	K6 (g)	0.0006(6)	0.0002(15)	0.026(2)	0.022(1)	neg.
	K5 (b)	0.126(4)	0.38(1)	2.4(1)	4.9(2)	14(1)
RB588A	Pure olivine analyses					
	K2	0.00027(9)	neg.	0.0012(4)	0.0001(2)	neg.
	K3	0.00027(8)	0.00013(10)	0.0016(2)	0.0003(1)	0.002(1)
	K5	neg.	0.0002(4)	0.0003(3)	0.0005(1)	neg.
	K6	0.00013(6)	neg.	0.0013(3)	0.00014(8)	neg.
Average $^{ol/melt}D_i$		**0.00017(13)**	**0.00007***(7)*	**0.0011(6)**	**0.00026(16)**	$0.0006^{(+9)}_{(-6)}$
	Crystal analyses compromised by contamination with glass or gas bubbles					
	K1 (g)	0.00007(5)	0.0002(2)	0.0017(2)	0.00130(9)	0.006(1)
	K4 (g)	0.00024(4)	0.0002(6)	0.0003(5)	0.0005(1)	0.006(3)
	K7 (b)	a.d.	a.d.	a.d.	a.d.	a.d.
RB588B	Pure olivine analyses					
	K1	0.0014(4	0.0000(0)	0.0023(3)	neg.	0.000(0)
	K3	0.0018(2)	0.00014(9)	0.0015(3)	neg.	0.014(4)
	K5	0.0022(4)	0.0001(2)	0.0039(5)	0.0005(1)	0.002(3)
	K6	neg.	0.00071(6)	0.0013(5)	neg.	neg.
Average $^{ol/melt}D_i$		**0.0013(9)**	**0.00025***(23)*	**0.0023(12)**	$0.00014^{(+2)}_{(-14)}$	$0.0006^{(+8)a}_{(-6)}$
	Crystal analyses compromised by contamination with glass or gas bubbles					
	K4 (b)	2.3(1)	6.9(3)	a.d.	a.d.	148(18)
RB589A	Pure olivine analyses					
	K2	0.0003(1)	0.0003(3)	0.0044(8)	0.0004(5)	neg.
	K5	0.0002(2)	neg.	0.004(1)	0.0015(13)	neg.
	K6	0.00050(9)	0.0016(4)	0.002(1)	0.0003(11)	neg.
Average $^{ol/melt}D_i$		**0.00034(14)**	**0.00063***(62)*	**0.0036(12)**	**0.00072(66)**	**0**
	Crystal analyses compromised by contamination with glass or gas bubbles					
	K3 (g)	0.00041(8)	0.0333(9)	0.0154(6)	0.0144(7)	0.012(4)
	K4 (g)	0.00001(11)	0.0239(9)	0.010(1)	0.004(1)	0.011(4)
	K7 (b)	a.d.	a.d.	a.d.	a.d.	a.d.
RB586A	Pure clinopyroxene analyses					
	K2	0.0005(3)	0.0007(2)	neg.	neg.	neg.
	K3	neg.	0.0005(2)	0.0021(3)	0.0006(1)	0.0009(18)
	K8	0.0001(1)	0.0008(2)	0.0011(4)	0.00042(5)	neg.
	K10	neg.	neg.	0.0013(3)	0.00017(8)	0.0000(0)
	K11	0.00040(7)	0.00008(12)	0.0010(2)	neg.	neg.
Average $^{cpx/melt}D_i$		**0.00020***(19)*	**0.00041(35)**	**0.0011(7)**	**0.00024***(22)*	$0.0002^{(+3)}_{(-2)}$

(continued on next page)

Table 3 (*continued*)

Sample	Raster	$^{min/melt}D_{He}$	$^{min/melt}D_{Ne}$	$^{min/melt}D_{Ar}$	$^{min/melt}D_{Kr}$	$^{min/melt}D_{Xe}$
	Crystal analyses compromised by contamination with glass or gas bubbles					
	K1 (g)	0.00005(14)	0.0005(2)	0.0008(2)	0.0006(2)	0.0145)
	K5 (g)	0.0052(3)	0.0031(3)	0.038(2)	0.037(3)	0.03(1)
	K6 (g)	0.00021(7)	0.0001(2)	0.0049(4)	0.0053(4)	0.003(1)
	K7 (g)	0.0005(1)	0.0004(3)	0.0052(4)	0.0046(5)	0.0009(9)
	K9 (g)	0.0009(1)	0.00035(8)	0.034(2)	0.032(3)	0.07(2)

The data represent the analysed partition coefficients, i.e., the quotient of noble gas concentrations of each crystal analysis and average noble gas concentration of glass of a particular sample.

Average $^{min/melt}D_i$ values given for each sample are calculated from pure crystal analyses. Uncertainties of the average values are either given as $1-\sigma$ standard deviation of the single values (bold numbers) or as the mean deviation (cursively written or indicated by an upper and lower limit). See Section 2.2 for explanation. Data of pure crystal analyses and the average $^{min/melt}D_i$ are shown in Fig. 4.

(b), (g): Crystal analyses were compromised by contamination due to either gas bubbles or glass, respectively, thus representing only apparent $^{min/melt}D_i$ values and are not included in the average value.

The preferred noble gas $^{min/melt}D_i$ values for olivine (RB588A) and clinopyroxene (RB586A) are highlighted.

Data from pits smaller than the average pit volume of the respective sample are not shown here and in Fig. 4 (i.e., RB587F: K2, K7, K8, K10; RB588B: K2; RB589A: K1; RB586A: K4).

neg. = negative values, set to zero for computing the average values (see Section 3.3 for explanation);

a.d. = above mass spectrometer range of detection.

[a] Without Xe of K3, since melt contribution cannot completely be excluded.

Table 4
Summary of average noble gas melt and crystal solubilities and the preferred noble gas partition coefficients for olivine and clinopyroxene

Sample	He	Ne	Ar	Kr	Xe
Noble gas solubilities in melt: 10^{-4} cm^3 STP/(g bar)					
N2SFo glass	12.0(3)	2.30(6)	0.258(9)	0.121(7)	0.040(2)
$Di_{60}Ab_{40}$ glass (RB586A)	15.7(2)	5.68(9)	0.682(11)	0.254(6)	0.079(8)
Noble gas solubilities in crystals: 10^{-8} cm^3 STP/(g bar)					
Olivine[a]	19(15)	1.6(1.6)	2.6(1.3)	0.28(17)	$0.19^{(+29)}_{(-19)}$
Clinopyroxene	31(29)	23(20)	7.5(5.1)	0.61(56)	$0.14^{(+22)}_{(-14)}$
$^{olivine/melt}D_i$[b]					
Preferred[c]	0.00017(13)	0.00007(7)	0.0011(6)	0.00026(16)	$0.0006^{(+9)}_{(-6)}$
Maximum[d]	0.00022(8)	0.00015(3)	0.0011(6)	0.00026(16)	0.0023(14)
$^{cpx/melt}D_i$					
Preferred[c]	0.00020(19)	0.00041(35)	0.0011(7)	0.00024(22)	$0.0002^{(+3)}_{(-2)}$
Maximum[d]	0.00033(18)	0.00051(31)	0.0014(5)	0.00040(22)	0.0004(4)

Data for N2SFo glass are average values including all single measurements of the five samples analysed. Data for RB586A are average values of 11 analyses. The uncertainties of the melt solubilities are the $1-\sigma$ standard error of the mean. The uncertainties of the crystal solubilities are as indicated in Table 3.

Partial pressures in bar of He, Ne, Ar, Kr, Xe are 268.2; 253.2; 272.3; 241.7; 54.6, respectively.

[a] Gas solubilities for olivine from RB588A.

[b] Data from RB588A.

[c] Preferred $^{min/melt}D_i$: data taken from Table 3. See Section 3.3 for explanation.

[d] Maximum value: only positive concentrations were used to calculate $^{min/melt}D_i$.

present in each sample as well as the number of ablation pits and their volume relative to the size of the pits in the glass are indicated in Table 2 and examples are shown in Figs. 2 and 3. Since the distribution of gas bubbles and melt inclusions was mapped in each crystal before lasering, they were avoided in most cases by precise positioning of laser pits. The abundances of noble gases measured in inclusion-free olivines and clinopyroxenes are very low. Thus, the blank contributed as much as 80–95% of the crystal analyses. In a few cases, noble gases had even slightly lower abundances than the respective blanks measured before and after the sample. In these cases the subsequently necessary blank subtraction led to "negative abundances" (Table A.2). This happened occasionally for all noble gases except ^{40}Ar, even if the volume of the respective crystal pit was comparatively large, (e.g., RB588A data in Table 3). The average noble gas solubilities in olivine and clinopyroxene revealed in this work are summarised in Table 4.

Some areas of olivine with gas bubbles were intentionally ablated and noble gas abundances measured in order to help in identification of analyses contaminated by gas inclusions. Ablation of gas bubbles lead to several orders of magnitude higher noble gas abundances with heavier noble gases enriched relatively to the lighter ones (see Section 3.4). In terms

of accidental inclusion of melt the main problem arose from the difficulty in estimating the thicknesses of the crystals and in ensuring that the ablation did not continue into underlying glass, a problem which resulted in several contaminated analyses as indicated in Table 2. As shown in Fig. 4A the contamination of crystal material by adjacent glass or melt inclusions enhances all noble gas abundances from He to Xe and simply increases the resultant $^{min/melt}D_i$ values towards unity parallel to the correct trend and without significant fractionation of the lighter from the heavier noble gases.

3.3. Derivation of noble gas mineral–melt partition coefficients

Individual noble gas $^{min/melt}D_i$ values were determined for each crystal analysis using the average noble gas abundance of the glass and are given in Table 3. An average $^{min/melt}D_i$ value was calculated for each noble gas for each sample, excluding those analyses that were contaminated by glass or fluid inclusions or where the ablated crystal raster volume was significantly smaller than that of other crystal rasters of the same sample as indicated in Table 3. For crystal analyses where the noble gas amounts were indistinguishable from blanks, a $^{min/melt}D_i$ value of zero was taken when computing average $^{min/melt}D_i$. In Fig. 4 the average $^{min/melt}D_i$ are given for all samples together with the values obtained for each crystal. The error of the average $^{min/melt}D^i$ is derived almost entirely from crystal analyses due to low gas amounts and consequently reflects analytical problems rather than sample inhomogeneities.

All noble gases are incompatible in olivine and clinopyroxene, with $^{ol,cpx/melt}D_i$ ranging from 10^{-4} to 4×10^{-3}. When $^{ol,cpx/melt}D_i$ values of the noble gas are comparable among all samples, Ar appears to be consistently more compatible than He, Ne, and Kr (Fig. 4).

In order to investigate the effects of minor elements of different charge on noble gas partitioning, we performed one experiment with spec-pure materials (RB587), one doped with 200 ppm Sc (RB588) and a third doped with 200 ppm Ti (RB589). Within uncertainty, the noble gas

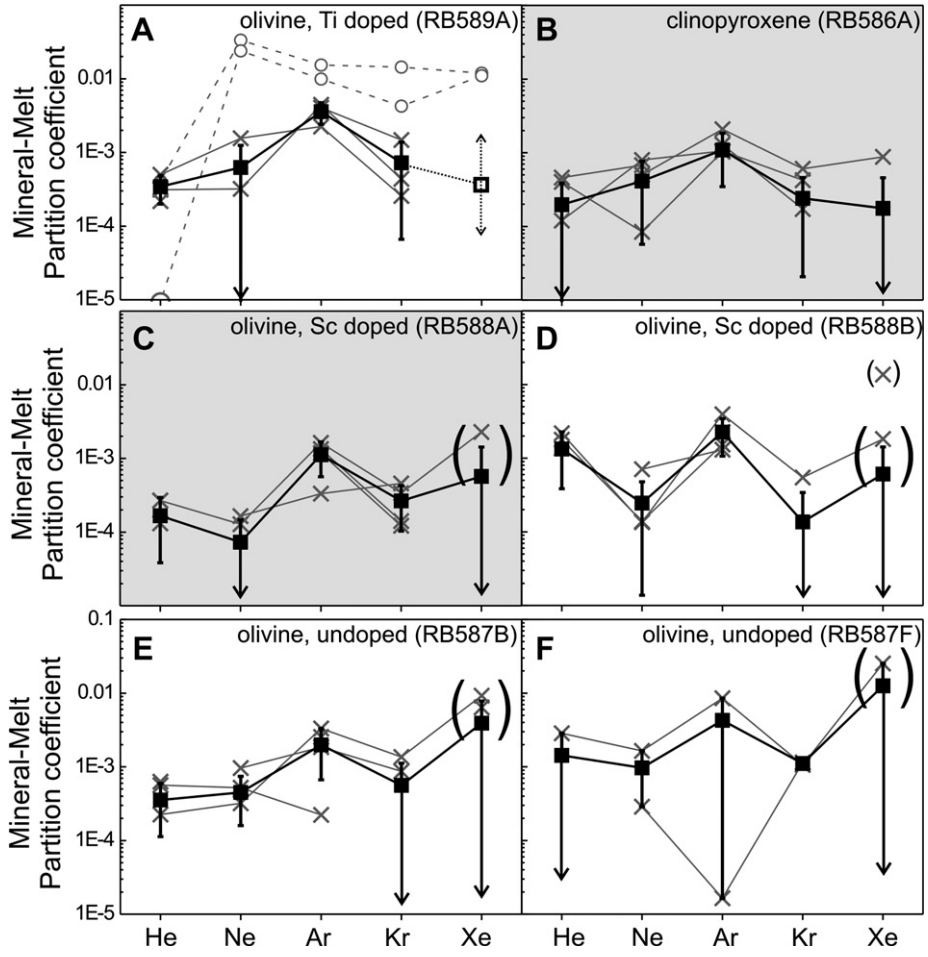

Fig. 4. (A–F) Noble gas olivine- and clinopyroxene–melt partition coefficients derived from the N2SFo and the $Di_{60}Ab_{40}$ experiments, respectively. In (A–F) $^{min/melt}D_i$ are shown for each crystal analysis (crosses) for each sample (errors have been omitted for clarity). From these values, average partition coefficients (black squares) were calculated (Table 3). The errors given for the average values are as indicated in Table 3. Arrows (here and in Figs. 7 and 8) indicate that lower limit of uncertainty is below the range of D values plotted. The samples that are most representative for noble gas partition coefficients between olivine and melt (C: RB588A) and clinopyroxene and melt (B: RB586A) are highlighted. For comparison, the $^{ol/melt}D_i$ of crystal analyses compromised by glass contamination (open circles) are shown in A (RB589A).

Please cite this article in press as: Heber, V.S. et al., Crystal–melt partitioning of noble gases (helium, neon, argon, ..., *Geochim. Cosmochim. Acta* (2007), doi:10.1016/j.gca.2006.11.010

partition coefficients for the three experiments are identical (Fig. 4). It seems therefore, the substitution of Sc or Ti as a possible charge-balancing mechanism has no observable effect on noble gas incorporation or partitioning in forsterite. The similarity of noble gas partitioning in olivine for different compositions is also supported by the data of Brooker et al. (1998) and Parman et al. (2005), who showed for Ar and He, respectively, that $^{ol/melt}D_i$ is similar for both Fe-free (and Ti-free) and Fe-bearing (±Ti) olivines, even though the latter might be expected to have a high concentration of vacancies associated with Fe^{3+}.

Our observations suggest that RB588A yields the most representative noble gas $^{ol/melt}D_i$ since this sample exhibits the largest crystal pit volumes (121% of that of the glass pit). Olivine–melt partition coefficients for He, Ne, Ar, Kr, and (Xe) at 0.1 GPa are 0.00017(13), 0.00007(7), 0.0011(6), 0.00026(16), and $0.0006^{(+9)}_{(-6)}$, respectively. The respective $^{cpx/melt}D_i$ values are 0.0002(2), 0.00041(35), 0.0011(7), 0.0002(2), and $0.0002^{(+3)}_{(-2)}$. If we include only "positive" individual D values in the calculation, the resulting average $^{min/melt}D_i$ values represent maximum values. The differences between the preferred and the maximum $^{min/melt}D_i$ values for olivine and clinopyroxene, summarised in Table 4, are small and well within the uncertainties, indicating that the method used to calculate the average $^{min/melt}D_i$ values is robust. Within uncertainty, the $^{cpx/melt}D_i$ values are identical to the olivine values (see below). Our data thus imply that noble gas partitioning is similar for both major mantle minerals clinopyroxene and olivine.

3.4. Influence of fluid inclusions on noble gas mineral–melt partition coefficients

Noble gas abundances for ablated pits in crystals that were deliberately targeted as containing fluid inclusions (Fig. 3C, pit K7), are several orders of magnitude higher than those measured in crystals without inclusions, resulting in extremely variable $^{min/melt}D_i$ up to $\gg 1$ (Fig. 5). For example, in RB587B, K8, two or three bubbles were sufficient to produce $^{min/melt}D_i$ above 1, indicating apparently compatible behaviour (Fig. 5). This effect can be quantified by considering a spherical gas bubble with a diameter of 5 μm. At a partial Ar pressure of 27 MPa, as used in the experiments, one bubble in a crystal contains about 4×10^{-9} cm^3 STP Ar and thus yields a much higher Ar abundance than the standard pit we used to measure noble gas composition in the glass, $60\times60\times4$ μm (2×10^{-10} cm^3 STP Ar). The contribution of fluid inclusions to the noble gas analyses can be independently identified from the noble gas abundance pattern, since inclusions are enriched in heavy noble gases with respect to the light ones (Fig. 5). The same approach can be used to evaluate the potential influence of the dark spots (~500 nm diameter) detected in olivine crystals, assuming them to be gas bubbles as discussed in Section 3.1. In comparison to the bubbles mentioned above they would have contributed about

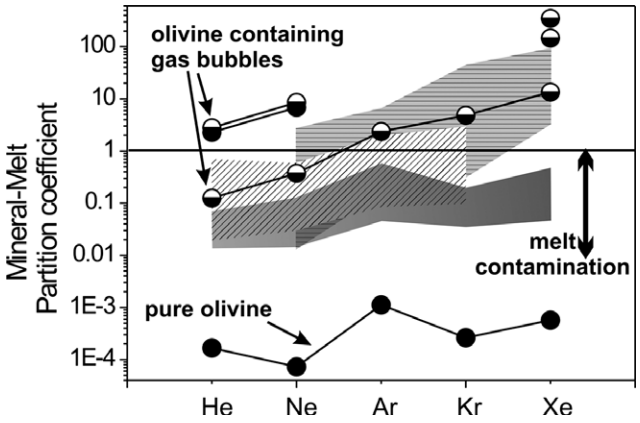

Fig. 5. A comparison of noble gas olivine–melt partition coefficients obtained from analyses of uncontaminated, "pure" olivine (solid circles, RB588A) with analyses of olivine that were contaminated by gas bubbles (half-filled circles). Olivine analyses contaminated by gas bubbles (K8 in RB587B, K5 in RB587F, K4 in RB588B) result in apparent noble gas partition coefficients that are four to six orders of magnitude larger depending on the number of gas bubbles. Note, that the heavy noble gases are preferentially distributed into the gas phase. For comparison literature partitioning data are given: Broadhurst et al. (1990, 1992) (horizontally hatched); Shibata et al. (1994) (diagonal hatched); Hiyagon and Ozima (1986) (dark grey). The first two of these studies show clear evidence for contamination either by fluid inclusions or by adsorption. The Hiyagon and Ozima study points to a contamination by glass due to imperfect separation indicated by the rather parallel translation of the pure olivine pattern.

1000 times less noble gas to a crystal analysis if ablated. At our experimental conditions a 500 nm bubble would contain 3.6×10^{-12} cm^3 STP Ar and 3.2×10^{-12} cm^3 STP Kr. If such a bubble were opened during a crystal analysis, it would result in an apparent $^{ol/melt}D_{Ar}$ of 0.026 and $^{ol/melt}D_{Kr}$ of 0.094. The result would therefore be a strong enrichment in heavy noble gases in the $^{min/melt}D_i$ vs. gas atomic radius pattern even at a very low concentration level. This is opposite to the observed pattern in these experiments. Since the olivine–melt partition coefficients given here follow $D_{Ar} > D_{Kr} \geqslant (D_{Xe})$ we can exclude bubble contamination as a major source of error in our analyses. This "bubble effect" may, however, account for the high $^{min/melt}D_i$ values increasing with atomic mass reported by other authors (Broadhurst et al., 1992; Shibata et al., 1994). Adsorption of noble gases on finely ground powders will also promote erroneously high $^{min/melt}D_i$ values together with enrichments in heavy noble gases (Ozima and Podosek, 2002), and could also account for the trends in data reported by Broadhurst et al. (1992) who used an olivine grain size of ~10 μm (Fig. 5).

4. Discussion

4.1. Noble gas solubilities in melt

The noble gas melt solubilities measured in our synthetic glass compositions (Table 4) agree with reported

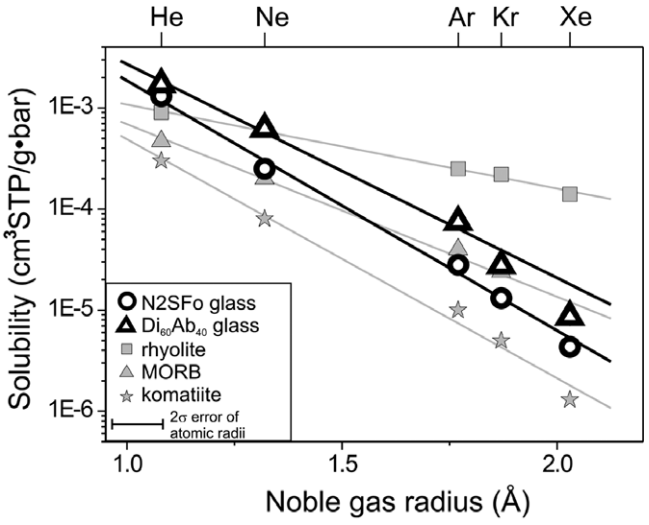

Fig. 6. Plot of average noble gas solubilities in saturated N2SFo and $Di_{60}Ab_{40}$ melt compositions as function of gas atom radius (Zhang and Xu, 1995). Uncertainties, as stated in Table 4, are within symbol size. Atomic radii error bar is for all noble gases, except Ne, for which it is half the size. Modelled solubilities, on the basis of ionic porosities, are shown for comparison for the typical natural melt compositions rhyolite, MORB, and komatiite (Carroll and Draper, 1994; Carroll and Stolper, 1993).

solubility data for other silicate melts (Hiyagon and Ozima, 1986; Lux, 1987; Broadhurst et al., 1992; Carroll and Stolper, 1993; Carroll et al., 1994; Brooker et al., 1998; Schmidt and Keppler, 2002; Miyazaki et al., 2004). Melt solubilities of He through Xe correlate with noble gas atomic radii from Zhang and Xu (1995) and decrease with increasing atomic size (Fig. 6) in agreement with, for example, Jambon et al. (1986) and Lux (1987). In Fig. 6 we compare our measured melt solubilities with modelled solubilities for ionic porosities representing typical natural melt compositions as rhyolite, MORB, and komatiite (Carroll and Stolper, 1993; Carroll and Draper, 1994). Noble gas solubilities of $Di_{60}Ab_{40}$ composition glass plot between those of MORB and rhyolite melt compositions and are higher than in the N2SFo glass. This latter observation reflects the higher amount of network-forming Si^{4+} and Al^{3+} in $Di_{60}Ab_{40}$ glass (64 wt% SiO_2 and 12 wt% Al_2O_3 compared to ~60 wt% SiO_2 in the N2SFo glass; Table 1), which leads to a higher degree of polymerisation and increasing number of "holes" available for noble gases in the melt structure (e.g., Carroll et al., 1994).

4.2. Noble gas partitioning data: comparison with previous data and incorporation mechanism

In this study we have determined noble gas mineral–melt partition coefficients for the mantle minerals olivine and clinopyroxene. Values are on the order of 10^{-4} for all noble gases, except Ar, which yields values close to 10^{-3}. Fig. 7 compares the new partition coefficients (summarised in Table 4) with those previously obtained by UV laser ablation as well as those obtained recently by crushing and melting experiments. The comparison shows that partitioning data obtained by UV laser ablation result in a relatively uniform database, confirming the incompatible behaviour of noble gases during melting and crystallisation.

The new partitioning results for noble gases in clinopyroxene are in good agreement with the data of Brooker et al. (2003a) with the exception of Kr and Xe, for which we find partition coefficients about an order of magnitude lower. The new values better fit the noble gas partitioning pattern defined by atomistic simulations (compare Fig. 8 with similar in Allan et al., 2003; Brooker et al., 2003a). We consider that the higher $^{cpx/melt}D_{Kr,Xe}$ values of Brooker et al. (2003a) (RB586) were probably due to incorporation of small fluid inclusions in the crystal analyses. The $^{cpx/melt}D_{Ar,Kr}$ obtained in this study are in very good agreement with the $^{cpx/melt}D_{Ar,Kr}$ given by Brooker et al. (1998) and Chamorro et al. (2002).

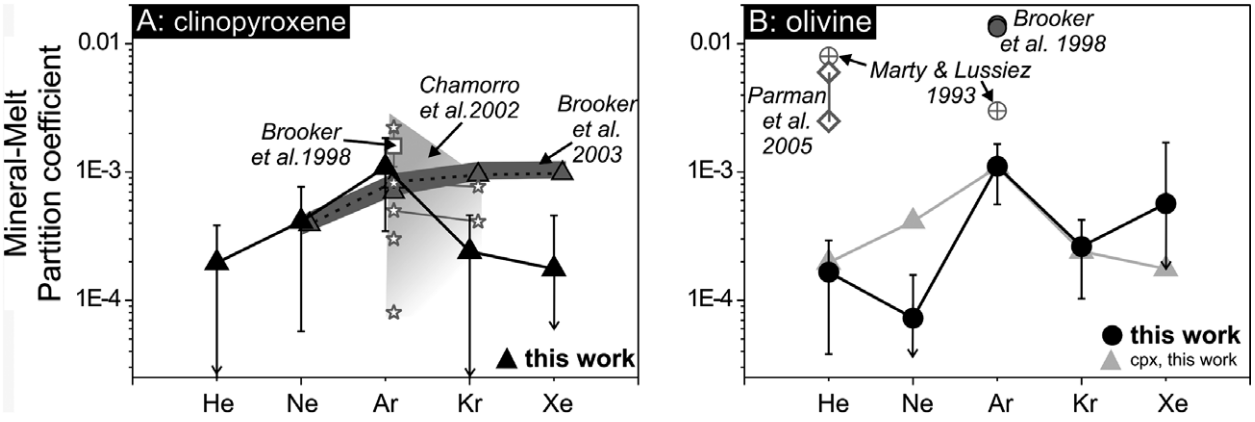

Fig. 7. Noble gas mineral–melt partition coefficients for clinopyroxene (A, solid triangles) and olivine (B, solid circles) obtained in this work are compared with previous data by UV laser ablation and crushing/melting. In B the $^{min/melt}D_i$ of clinopyroxene (grey solid triangles) are shown again together with the olivine data for a better comparison of both data sets. Error bars for literature data have been omitted for clarity. Literature UV laser ablation data: A: Chamorro et al. (2002) (open stars), Brooker et al. (1998) (open square), Brooker et al. (2003a) (grey solid triangles); B: Brooker et al. (1998) (grey solid circle). Literature crushing/melting data: B: Parman et al. (2005) (open diamonds), Marty and Lussiez (1993) (open circles with cross).

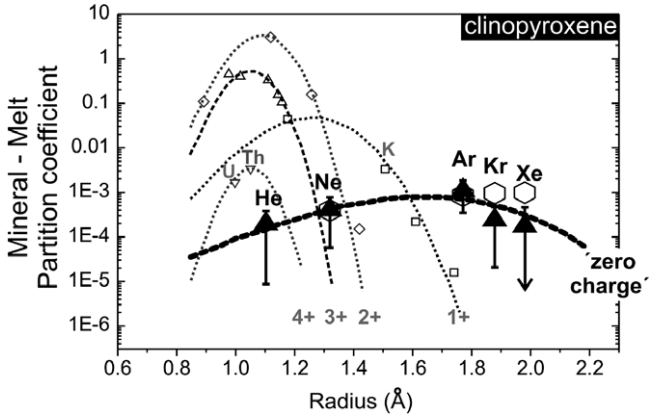

Fig. 8. Plot of clinopyroxene–melt partition coefficients vs. ionic radius for major and trace elements (at valency indicated) and noble gases. The diagram was adapted from Brooker et al. (2003a) and compares the noble gas partition coefficients obtained in this work (filled triangles) with the data from that study (open hexagon). Arrows indicate that lower limit of uncertainty is below the range of D values plotted. The newly fitted 'zero charge' parabola has parameters of $d_0 = 0.00082$, $E = 14.13$ and $r_0 = 1.641$ for comparison with the values stated in Brooker et al. (2003a).

The new noble gas partitioning values for olivine measured in this work are all more than one order of magnitude lower than those previously reported (Marty and Lussiez, 1993; Valbracht et al., 1994; Brooker et al., 1998; Parman et al., 2005). In Brooker et al. (1998), Marty and Lussiez (1993) and Valbracht et al. (1994) partition coefficients were identified as maximum values since the contribution of melt inclusions or adjacent glass during crystal analyses could not be fully excluded. In the present study, as discussed above, we were able to minimise glass contamination of the analyses through the greatly improved spatial resolution of our laser and optical system. We therefore consider the new results to be superior to those we presented earlier (Brooker et al., 1998).

An alternative approach to olivine–melt partitioning of He was employed by Parman et al. (2005). These authors measured the apparent solubility of He in olivine crystals ($\sim 3 \times 10^{-6}$ cm^3 STP/(g bar)) in the absence of melt and calculated $^{ol/melt}D_{He}$ using published He solubilities in basaltic melts. Using this approach they avoided the possibility of adding high amounts of He to a crystal analysis from adjacent glass. Although we considered their approach complementary to ours, we should point out that there are still several potential problems with the Parman et al. (2005) partitioning values. First, the olivine does not have its point defect concentrations equilibrated with the melt and, as discussed below, point defects almost certainly play an important role in noble gas incorporation in the olivine structure. Second, exposure of olivine grains to a concentrated He (50%) atmosphere at high temperature may cause an incorporation of He in extended defects near the grain surfaces and in nanopores (cf. Watson and Cherniak, 2003). Several diffusion studies of crystals exposed to noble gas atmospheres at high temperature have revealed that noble gases are highly abundant in the uppermost several hundred nm, with concentrations one to two orders of magnitude higher than in the deeper layers. Concentrations in this outer layer could not be included in the modelling of diffusion profiles. This phenomenon has been observed for Ar in feldspar (Wartho et al., 1999), He in garnet (Roberts, 1999), and for other noble gases in olivine (Heber et al., 2004). As shown by Roselieb et al. (1997), this 'surface contamination' can reside in 'hot spots' on the surface possibly related to healed fractures and thus may not scale with surface area. Finally, diffusion data of Heber et al. (2004) ($D^{He}_{Ol,\ 1000\,°C}$: $1–2 \times 10^{-15}$ cm^2/s) extrapolated to 1350 °C using the activation energy of Trull and Kurz (1993) suggest that volume diffusion of He in olivine would have reached an average depth of 50 μm under Parman et al.'s experimental conditions (21 days at 1350 °C). This suggests that the grains may not have achieved equilibrium despite the observation of Parman et al. (2005) that grains of 100 μm diameter and 1 mm yield similar apparent solubility.

The most striking features of Figs. 7 and 8 are first that partition coefficients for olivine and clinopyroxene are very similar (Fig. 7) and secondly that there is very little dependence of partitioning on atomic number or atomic radius (Figs. 7 and 8). These observations lead us to consider how noble gas atoms are incorporated in the crystal structures of silicates. Incorporation of an atom of zero charge in the structure must involve the occurrence of defects, either equilibrium (point) defects or disequilibrium extended defects such as surfaces or dislocations. The aim of our study was to measure equilibrium partitioning so we minimised the presence of disequilibrium defects in the same way as employed in numerous other trace element partitioning studies (e.g., Blundy and Wood, 1994) by growing crystals slowly from silicate melt. Although our technique does not permit an experimental 'reversal' of partitioning, the reproducibility of our results (Table 3) suggests that equilibrium was approached. We therefore consider that point defects dominate the results and that extended disequilibrium defects are relatively unimportant.

At equilibrium, all silicates contain vacancies which can be occupied by noble gas atoms. Some of these are interstitial positions which are normally vacant even in the 'perfect' structure while others are cation or anion vacancies whose concentrations depend on the chemical environment, pressure and temperature. Of the latter, both theoretical (e.g., Smyth and Stocker, 1975) and experimental studies (Nakamura and Schmalzried, 1983) indicate that in olivine the dominant vacancies are in the large cation (Mg, Fe) positions. Thus, noble gas atoms should enter either interstitial positions or the large M-site positions. In a previous paper (Brooker et al., 2003a) we investigated the dissolution of noble gas atoms into clinopyroxene using atomistic simulations based on the GULP computer program of Gale (1997). The simulations are consistent with the favoured substitution for Ar, Kr and Xe being into the large M2 cation site while the smaller Ne (and by extension He) prefer an interstitial position. In principle, there-

Please cite this article in press as: Heber, V.S. et al., Crystal–melt partitioning of noble gases (helium, neon, argon, ..., *Geochim. Cosmochim. Acta* (2007), doi:10.1016/j.gca.2006.11.010

fore the important defects in clinopyroxene and olivine are the same, interstitial vacancies and M-site cation vacancies.

Brooker et al. (2003a) went a step further in the interpretation of their simulations and experimental (noble gas) data by relating the results to the lattice strain model of Blundy and Wood (1994) for trace element partitioning. This predicts that ions substituting into a given cation site will have crystal–melt partition coefficients which, for each cation charge, define a parabola as a function of ionic radius. Fig. 8 shows such parabolae for 1+, 2+, 3+ and 4+ ions substituting into the large cation site in clinopyroxene from experiment RB586. Empirically, Blundy and Wood (1994) observed that, for fixed cation–oxygen distance d (Å) the curvature of the parabola, as defined by E, the apparent Young's Modulus of the site, is an approximately linear function of the charge on the trace ion Z_c:

$$E \approx 1125\frac{Z_c}{d^3}\ \text{GPa}$$

Thus, ions of progressively lower charge should exhibit lower and lower E more and more 'open' parabolae as shown in Fig. 8. Wood and Blundy (2001) used this empirical observation to propose that 'ions' of charge zero, such as the noble gases should substitute with E close to zero and should hence have partitioning which is essentially independent of ionic radius i.e., the 'parabola' opens out to a straight line. Figs. 7 and 8 show that this is essentially what is observed for olivine and clinopyroxene (see also Brooker et al., 2003a).

The lack of dependence of noble gas partition coefficient on atomic radius (Figs. 7 and 8) was taken by Brooker et al. (2003a) to support the idea that noble gases partition as if they were trace ions of zero charge. This was proposed in the context of noble gases entering vacancies in the M2 site of clinopyroxene, but should also apply in the case of substitution at interstitial vacancies since these must relax around the substituent atoms in a similar manner to the cation vacancies. Two of our experiments (RB588 and RB589) were aimed at discriminating the nature of the defect which incorporates noble gas atoms in olivine. By adding Sc^{3+}, an ion of virtually the same size as Mg^{2+}, to olivine (RB588) we should have created vacancies in the magnesium positions because charge balance requires that the substitution be as follows:

$$3Mg^{2+} \leftrightarrow 2Sc^{3+} + V_{Mg}$$

where V_{Mg} denotes a magnesium vacancy. If noble gases were to preferentially enter magnesium vacancies then we would expect that this experiment (RB588) would produce higher partition coefficients than the spec-pure experiment RB587. In fact, there is no detectable difference in partition coefficients (Table 3). Assuming the starting materials for RB587 were 'spec-pure', this implies that noble gases do not enter substitutional (extrinsic) cation vacancies in the olivine structure. The result is supported by experiment RB589 in which Ti^{4+} was added. No detectable change in partition coefficients was observed. Our data therefore are most consistent with noble gases entering interstitial, normally vacant, positions in the olivine structure. The implication is that noble gases enter positions which are present in all olivines independent of composition and that similar partitioning behaviour should be observed for all olivines. This is consistent with the observations of Parman et al. (2005) who found no difference in He solubility between pure forsterite and Mg_{90} olivine under similar conditions. Clinopyroxene, for which we have a wider range of data, behaves in a similar fashion. Clinopyroxenes along the join diopside-jadeite exhibit virtually identical crystal–melt partition coefficients for noble gases (Brooker et al., 2003a). Addition of Fe makes no apparent difference according to the data of Brooker et al. (1998) and Chamorro et al. (2002), supporting the hypothesis that partitioning is into sites which are vacant in all clinopyroxenes.

4.3. Implications for noble gas compositions of mantle-derived melts

The low ${}^{\text{min/melt}}D_i$ values for noble gases indicate that they all behave in a strongly incompatible fashion. Despite this, the partition coefficients for noble gases into clinopyroxene are similar to those of the strongly lithophile elements U, Th, and K (Fig. 8). For olivine, our measured partition coefficients for the noble gases are one to two orders of magnitude greater than the observed published values for U, Th, and K (Beattie, 1993; Hart and Brooks, 1974; Wood et al., 1999). Preliminary ion probe data for olivine and melt in sample RB571 (grown at the same conditions as olivines in this study; see Section 2.1.1) also suggest low ${}^{\text{ol/melt}}D_K$ of $<1.6\times10^{-4}$ and ${}^{\text{ol/melt}}D_{Th}$ of 9×10^{-6}. The data support the suggestion that a small but significant amount of primordial noble gases must have been preferentially retained in the mantle during crustal extraction, especially if this involved batch rather than fractional melting and cpx is exhausted from the mantle assemblage. Major differences between asthenosphere- and plume-derived basalts (MORB and OIB, respectively) are generally the abundance ratios of primordial to radiogenic noble gas isotopes, e.g., $^3He/^4He$, $^{22}Ne/^{21}Ne$ and $^{36}Ar/^{40}Ar$, which are higher in OIB than in MORB. The common interpretation that OIB derive from a largely non-degassed, relatively isolated mantle source, is, however, the subject of considerable debate due to the low He abundances in OIB samples compared to MORB (e.g., Albarède, 1998; Farley and Neroda, 1998; Ozima and Igarashi, 2000; Meibom et al., 2003) and the growing evidence of whole mantle mixing (e.g., van der Hilst et al., 1997; Bijwaard and Spakman, 1998; Fukao et al., 2001). Key to this debate is the general assumption that noble gases are more incompatible than the parent elements of their radiogenic isotopes (U, Th, and K), such that primordial ^3He, ^{22}Ne, and ^{36}Ar are completely stripped from the mantle during melt extraction, leaving a source dominated by the residual radioactive parents, U, Th, and K. These radioactive elements should, in

Please cite this article in press as: Heber, V.S. et al., Crystal–melt partitioning of noble gases (helium, neon, argon, ..., *Geochim. Cosmochim. Acta* (2007), doi:10.1016/j.gca.2006.11.010

this model, subsequently decay to produce high ratios of $^{4}He/^{3}He$, $^{21}Ne/^{22}Ne$ and $^{40}Ar/^{36}Ar$. In practical terms, this requires noble gas partition coefficients less than around 10^{-6}, far lower than measured in this study. Our new data suggest that the noble gases are less incompatible than their radioactive parents during mantle melting, leading to a re-evaluation of the geochemical relationships between parent and daughter isotopes.

Brooker et al. (2003b) and Parman et al. (2005) have used the measured partition coefficients for noble gases and radioactive parents to show that the ''primordial'' He signature in OIB could result from re-melting of a previously melted, recycled, and degassed lithosphere. If we make the reasonable assumption that noble gas partitioning into orthopyroxene is similar to that observed for clinopyroxene and olivine, partial melting of the mantle should lead to preferential extraction of K, U and Th relative to the noble gases. The residual depleted reservoir would have a relatively undisturbed primordial/radiogenic $^{3}He/^{4}He$ ratio and, with time, due to preferential extraction of the U and Th parents, a lower integrated ^{4}He ingrowth. The resulting, relatively weak ingrowth of radiogenic ^{4}He, ^{21}Ne, and ^{40}Ar in dunitic and harzburgitic residue will preserve a noble gas isotope signature high in the primordial isotopes relative to the radiogenic isotopes. Recycling of this previously depleted residual lithosphere into source regions of OIB provides an alternative explanation for the apparently high primordial $^{3}He/^{4}He$ signatures in OIB and also explains the low noble gas abundances. The same model can equally be applied to argon isotope ratios. The isotopic signature in OIB is characterised by a less radiogenic ingrowth compared to MORB ($^{40}Ar/^{36}Ar$ up to about 40,000 in MORB and up to 8000 in OIB (Graham, 2002)), in agreement with an OIB source that is depleted in radioactive K compared to primordial Ar and lower in total Ar. Many trace element and isotopic features of OIB suggest that recycling of oceanic crust and lithosphere plays an important role in the creation of mantle heterogeneities (Hofmann, 1997; van Keken et al., 2002; Class and Goldstein, 2005). Our noble gas partitioning data indicate that recycling of depleted ancient lithosphere is also able to generate the 'undegassed' noble gas isotope signature of OIB.

5. Conclusion

We have shown that UV laser ablation is capable of analysing noble gases in laboratory grown coexisting crystals and melt to obtain partition coefficients. Most important in this respect, since crystal/melt partition coefficients of noble gases are very low, has been the development of techniques to grow crystals virtually free of melt and fluid inclusions. Mineral–melt partition coefficients obtained for the olivine–melt system for He, Ne, Ar, Kr, and (Xe) are 0.00017(13), 0.00007(7), 0.0011(6), 0.00026(16), and $0.0006^{(+9)}_{(-6)}$ and the clinopyroxene–melt system 0.0002(2), 0.00041(35), 0.0011(7), 0.0002(2), and $0.0002^{(+3)}_{(-2)}$, respectively. The data confirm the incompatible behaviour of noble gases for both olivine and clinopyroxene. Although the noble gases are incompatible, our data indicate that significant amounts of all noble gases can be retained in the mantle during partial melting. The data also show that the noble gases are likely to have similar incompatibilities in many major upper mantle phases and are not fractionated (relative to each other) during melting and crystallization involving olivine, clinopyroxene and (probably) orthopyroxene. A comparison of relative partitioning behaviour of noble gases and their radioactive parents during partial melting indicates that the noble gas isotopic signatures of OIB can be achieved by recycling of previously melted (depleted) mantle source.

Acknowledgments

This manuscript was greatly improved by comments from referees Steve Parman, Pete Burnard and an anonymous reviewer. We thank Rainer Wieler enabling us to calibrate our calibration bottle and Bernard Marty for discussion and correction of the manuscript. We acknowledge Richard Chater from the Imperial College for access to the interferometer. V.S. Heber acknowledges the financial support provided through the European Community's Human Potential Programme under contract HPRN-CT-2002-000211 (EUROMELT) and the EUROMELT network coordinator Kevin W. Burton. R. Brooker, S. Kelley and B. Wood acknowledge the financial support provided by the NERC (NER/A/S/2001/00464).

Associate editor: Jun-ichi Matsuda

Appendix A

A.1. Achievement of equilibrium

Equilibration of noble gases between crystal and melt requires: (i) noble gases to be homogeneously distributed in the starting melt at the initiation of crystal growth, and (ii) equilibrium growth of crystals under a carefully controlled T path (Brooker et al., 1998). The first criterion was particularly important in our case because of the relatively low temperatures we used (1165 °C, 1285 °C) compared to previous experiments (Brooker et al., 1998, 2003a; Chamorro et al., 2002) that would have prevented diffusive equilibration over long distances (see below).

Initially, equilibration times were calculated using Ar diffusion coefficients (D_{Ar}) estimated from the work of Lux (1987). Accordingly, Ar would have diffused about 4.5 mm into the $Di_{60}Ab_{40}$ melt column after 9 h at 1285 °C (computed as $x = \sqrt{Dt}$ where x is the average diffusive length scale and t is the run duration in seconds). However, recent D_{Ar} data for a glass of comparable composition from Nowak et al. (2004) suggest that Ar would only have diffused into the upper 0.5 mm under these conditions ($D_{Ar,\ andesitic,1285°C}$ 7×10^{-8} cm/s^2). To investigate the noble gas diffusion in the $Di_{60}Ab_{40}$ melt we ran the test

sample RB585 for 9 h. The 7 mm long glass column was sectioned at 1.1 and 5.7 mm below the gas–melt interface. Noble gas abundances were measured at the resultant intersection planes. The data show that 9 h were sufficient to equilibrate He in the whole glass. The ratio of He and to the other noble gases indicates that Ne, Ar, Kr, and Xe had reached 90 to 100%, 9%, 0.4%, and 0.02% at 5.7 mm, respectively, compared to their abundances at 1.1 mm depth. Model concentration vs. depth curves calculated using the noble gas abundances at 5.7 mm as limiting factor are consistent with the assumption that Ar, Kr, and Xe reached 80%, 60%, and 45–50%, respectively, of saturation conditions at 1.1 mm. The corresponding Ar diffusion coefficient for the $Di_{60}Ab_{40}$ glass is about 1.6×10^{-6} cm/s^2 at 1285 °C. This diffusion coefficient is indeed somewhat lower than the value extrapolated using data from Lux (1987) but consistent with the range of D_{Ar} of 0.2-9 $\times 10^{-7}$ cm/s^2 proposed by Hazelton et al. (2003). Our results strongly suggest, therefore, a faster diffusion rate for Ar than the one estimated by Nowak et al. (2004). A reason for the difference might be the extrapolation of the Nowak data determined between 1350 °C and 1500 °C to lower temperatures used in our experiments. We believe that in sample RB586 most of the noble gases approached equilibrium concentrations because the much shorter melt column (1.7 mm) was much longer exposed to the noble gas pressure medium (20 h in total) before crystal growth started. Crystals also mainly grew at the gas–melt interface (as reported in Brooker et al., 2003a) and down the upper sides of the capsule. Crystals at the gas–melt interface are certainly equilibrated with respect to Xe, although this may not be the case for all crystals included in this study. The gradient in the test glass also suggests that convective mixing did not take place within the $Di_{60}Ab_{40}$ melt, which is consistent with the observation of Nowak et al. (2004).

Applying Nowak et al.'s (2004) data to the N2SFo experiment we find that Ar would have diffused only about 0.25 mm into the melt column after 20 h at 1165–1035 °C. However, as for the case of $Di_{60}Ab_{40}$, we believe that extrapolating Nowak et al.'s diffusion data to the lower temperature conditions used in our experiments leads to too slow estimated diffusion rates. One reason could be the low viscosity of the N2SFo melt at low temperatures, indicated by the high ratio of non-bridging oxygens per tetrahedral cation (NBO/T = 1.56). This is supported by a positive correlation of Ar diffusion vs. NBO/T for several melt compositions (Nowak et al., 2004). More importantly, the samples of the N2SFo experiments were loaded as glass powder (grain size 25 μm) into 3 mm capsules and were exposed to the high-pressure noble gas medium before melting. On melting, this reduced to half capsule volume (1.7 mm melt column) to give a melt initially full of noble gas bubbles. After some time (<5 h) these bubbles escape to the gas–melt interface. The duration of the initial melt equilibrium period for the N2SFo experiments (RB587–589) was 1 h at 1165 °C, followed by 3 h between 1165 and 1040 °C. A further 16 h of slow cooling then elapsed before crystals began to grow at ~1035 °C. For a grain size of 25 μm even conservatively used Nowak et al.'s (2004) diffusion coefficients predict Ar equilibration in less than 10 min at 1165 °C. Also, the low viscosity and movement of bubbles should have promoted convective/turbulent mixing. Equilibrium of noble gases between the gas phase and the melt is independently supported by the fact that all noble gases, including Xe, have similar abundances in different aliquots of all N2SFo glasses (Table A.2) after 100 h (the overall run duration) which is evident from the small uncertainties associated with solubility data (Table 4).

The achievement of noble gas equilibration for the growing crystal interface is more difficult to assess. If crystals grew in non-equilibrium conditions, then one might expect to observe a large range of $^{min/melt}D_i$ values for a given noble gas, and among different noble gases. This is, however, difficult to evaluate because errors on the single $^{min/melt}D_i$ values in this study are relatively high as a result of the low gas concentrations in crystals. However, we observe that the $^{min/melt}D_i$ of different noble gases show variations consistent with predictions based on theoretical considerations of trace element partitioning (the open parabola, Brooker et al., 2003a). Furthermore, heavy noble gas $^{min/melt}D_i$ values are comparable to those of lighter noble gases, as expected from these considerations and there is little doubt that equilibrium was reached in the case of the lighter gases.

A.2. Diffusive loss of He from glass

From a depth profile analysis in a RB588 aliquot (RB588C, data of this analysis are given in Table A.1) and its duration of storage at room temperature before analysis (153 days) we computed a He diffusion coefficient for N2SFo glasses at 23 °C of 2.4×10^{-14} cm^2/s using the diffusion equation for transport normal to surface of a solid assuming a semi-infinite medium:

$$c = c_0 \left[\mathrm{erf}\left(\frac{x}{4Dt} \right) \right]$$

Fig. A.1 shows the concentration profile of He in comparison to Ne as well as the error function fitted through the He data. The resulting He diffusion coefficient is within

Table A.1
He, Ne, and Ar abundances from a depth profile in N2SFo glass (RB588C, R14)

Layer	Cumulated depth (μm)	Area (μm^2)	^{4}He	^{22}Ne	^{40}Ar
r14-1	2.9	10,040	17.0(1)	5.74(2)	38.30(5)
r14-2	7.6	10,040	44.5(5)	5.16(1)	35.96(3)
r14-3	12.3	10,040	54.8(1)	5.00(4)	34.47(3)
r14-4	17.0	10,040	65.9(1)	4.70(1)	31.92(6)
r14-5	21.6	10,040	64.3(2)	4.20(1)	28.33(5)
r14-6	26.3	10,040	63.9(5)	3.75(1)	25.68(5)

Abundances given in 10^{+6} V/g. See Appendix A.2 for explanation.

Table A.2
Measured noble gas abundances

Analyses	Ablated volume (μm^3)	^{4}He	^{22}Ne	^{40}Ar	^{84}Kr	^{132}Xe
A.2.1. RB588A						
Glass analyses (single raster areas)						
R1	14,100	272(2)	53.55(20)	66.81(13)	14.85(4)	0.535(9)
R2	15,800	263(2)	50.70(25)	60.97(20)	13.81(6)	0.429(11)
R3	17,185	278(2)	49.40(14)	61.38(16)	14.34(4)	0.468(5)
R4	16,600	302(2)	51.87(7)	63.04(8)	14.68(1)	0.513(5)
R6	18,100	277(2)	50.10(7)	62.22(6)	15.01(2)	0.496(5)
R7	15,088	266(2)	51.31(17)	63.87(12)	14.12(5)	0.532(3)
R8	14,900	258(2)	50.09(14)	61.84(18)	13.66(1)	0.476(9)
R9	14,800	143(2)	49.16(4)	61.98(15)	14.72(2)	0.498(9)
R11	15,100	249(3)	50.31(12)	65.84(4)	15.09(5)	0.535(6)
R12 a	20,231	2.8(4)	17.68(9)	65.01(2)	13.82(2)	0.515(8)
R13 a	19,400	1.8(5)	14.94(6)	62.78(5)	13.31(3)	0.506(5)
R14 a	20,000	1.8(5)	16.43(6)	63.63(6)	14.60(6)	0.484(3)
Depth profiles in glass						
R5.1		103(1)	27.2(3)	32.01(6)	7.60(7)	0.251(13)
R5.2		210(1)	56.8(1)	64.17(15)	13.98(3)	0.477(8)
R5.3		283(3)	62.1(1)	75.41(10)	17.20(3)	0.586(8)
R5.4		346(2)	58.2(2)	70.49(6)	16.18(3)	0.612(5)
R5.5		417(1)	55.4(1)	66.92(14)	15.29(3)	0.573(7)
R5.6		511(4)	55.2(2)	65.89(3)	15.00(3)	0.582(10)
R5.7		576(2)	53.4(1)	65.85(7)	15.00(2)	0.556(8)
R5.8		677(3)	51.9(3)	63.47(3)	14.24(3)	0.508(8)
Total	*67,800*	*390(2)*	*52.5(2)*	*63.03(8)*	*14.31(3)*	*0.518(8)*
R10.1		86(2)	26.9(3)	33.46(10)	7.06(1)	0.192(3)
R10.2		148(3)	45.1(2)	52.76(13)	10.85(5)	0.375(8)
R10.3		253(5)	57.9(3)	68.29(14)	14.46(3)	0.521(12)
R10.4		289(2)	61.0(1)	77.58(11)	16.42(4)	0.536(12)
R10.5		311(3)	56.7(1)	72.82(14)	15.39(5)	0.524(6)
R10.6		384(2)	59.1(3)	73.11(17)	15.47(6)	0.521(7)
R10.7		408(6)	54.0(2)	69.37(6)	14.59(5)	0.557(9)
R10.8		474(3)	52.4(2)	67.76(12)	14.47(3)	0.554(8)
Total	*60,900*	*294(3)*	*51.6(2)*	*64.39(12)*	*13.59(4)*	*0.472(8)*
R15.1 a		6.7(6)	2.6(1)	35.96(8)	7.44(4)	0.276(9)
R15.2 a		0.7(6)	12.4(1)	72.20(6)	14.59(6)	0.481(17)
R15.3 a		1.1(7)	17.2(2)	71.67(18)	14.99(3)	0.489(17)
R15.4 a		2.8(5)	21.5(2)	65.49(17)	13.60(5)	0.395(8)
Total	*40,900*	*2.8(6)*	*13.4(1)*	*61.33(12)*	*12.66(5)*	*0.410(13)*
Olivine analyses						
K1	24,600	0.2(2)	0.010(9)	0.11(1)	0.019(1)	0.0029(5)
K2	23,800	0.8(3)	−0.022(7)	0.07(3)	0.002(3)	−0.002(2)
K3	28,600	0.8(2)	0.007(5)	0.10(1)	0.005(2)	0.0011(7)
K4	17,200	0.7(1)	0.012(28)	0.02(3)	0.007(2)	0.0032(14)
K5	19,600	−0.3(1)	0.008(19)	0.02(2)	0.007(1)	−0.003(1)
K6	24,100	0.4(2)	−0.010(5)	0.08(2)	0.002(1)	−0.002(1)
K7		a.d.	a.d.	a.d.	a.d.	a.d.
A.2.2. RB588B						
Glass analyses (single raster areas)						
R1	16,200	170(4)	53.0(2)	65.44(13)	14.12(5)	0.464(7)
R2	15,900	177(2)	52.9(2)	69.28(12)	15.08(3)	0.497(13)
R3	16,800	196(4)	52.8(3)	61.80(23)	14.68(4)	0.544(6)
R4	15,700	197(3)	50.3(2)	63.74(8)	15.36(3)	0.580(4)
R6	15,700	251(4)	52.5(3)	66.31(11)	16.01(5)	0.536(1)
R7	14,700	245(4)	50.9(1)	68.55(18)	16.72(3)	0.644(7)
R9	14,000	222(3)	57.5(4)	70.71(15)	16.27(5)	0.619(1)
R10	14,920	227(3)	50.1(4)	70.97(14)	17.61(4)	0.629(9)
R11 a	15,300	75(2)	43.4(4)	64.57(10)	15.08(2)	0.591(6)
R12 b	12,700	21(2)	27.5(2)	62.45(16)	15.19(3)	0.589(16)
R13 b	13,200	16(2)	25.8(2)	67.01(11)	16.63(2)	0.731(12)

(*continued on next page*)

Table A.2 (*continued*)

Analyses	Ablated volume (μm^3)	^{4}He	^{22}Ne	^{40}Ar	^{84}Kr	^{132}Xe
Depth profile in glass						
R8.1		77(8)	27.9(4)	37.32(17)	9.04(4)	0.344(11)
R8.2		164(7)	55.7(6)	65.31(5)	15.84(6)	0.542(7)
R8.3		244(15)	65.31(4)	82.22(20)	19.65(3)	0.664(25)
R8.4		247(7)	58.3(3)	74.15(12)	17.80(5)	0.704(19)
R8.5		295(9)	56.2(4)	69.96(24)	17.17(10)	0.679(15)
R8.6		328(9)	53.2(3)	69.06(10)	16.82(10)	0.656(18)
R8.7		409(5)	51.7(2)	67.14(7)	16.30(4)	0.518(12)
Total	*56,200*	*252(9)*	*52.6(3)*	*66.45(14)*	*16.09(6)*	*0.587(15)*
Olivine analyses						
K1	12,100	4.3(1.1)	0	0.15(2)	−0.006(3)	0
K2	6130	−11.1(3.2)	0.025(26)	0.85(5)	0.013(5)	0.001(2)
K1	12,100	4.3(1.1)	0	0.15(2)	−0.006(3)	0
K2	6130	−11.1(3.2)	0.025(26)	0.85(5)	0.013(5)	0.001(2)
K3	15,200	5.6(7)	0.007(5)	0.10(2)	−0.002(1)	0.008(2)
K4	18,100	7194	361	a.d.	a.d.	86
K5	12,603	6.8(1.4)	0.007(12)	0.26(3)	0.009(2)	0.001(2)
K6	17,500	−0.9(6)	0.037(2)	0.09(3)	−0.004(1)	−0.002(0)
A.2.3. RB589A						
Glass analyses (single raster areas)						
R1	18,600	423(6)	57.8(3)	75.84(12)	17.136(5)	0.554(5)
R2	18,900	360(5)	59.6(3)	77.58(11)	17.75(4)	0.562(19)
R3	19,200	331(2)	58.1(1)	74.08(12)	16.98(3)	0.540(5)
R4	20,200	360(2)	58.9(6)	75.98(12)	17.56(4)	0.565(4)
R6	20,747	384(2)	59.1(2)	75.49(7)	17.54(6)	0.578(10)
R7	19,200	319(16)	58.8(3)	76.08(29)	17.36(11)	0.589(28)
R8	19,200	355(8)	60.9(2)	78.03(11)	17.51(2)	0.560(15)
R9	19,900	345(6)	58.5(4)	74.66(26)	17.38(5)	0.569(8)
R10 a	20,000	0.4(6)	25.14(5)	77.46(6)	17.56(3)	0.607(6)
R11 a	19,600	0.8(5)	24.2(2)	76.39(12)	17.48(3)	0.585(5)
Depth profile in glass						
R5.1		72(3)	26.9(2)	36.18(9)	8.06(1)	0.279(7)
R5.2		190(2)	56.6(3)	68.58(14)	15.61(3)	0.480(5)
R5.3		309(3)	69.3(2)	90.01(11)	20.23(3)	0.596(12)
R5.4		403(2)	62.9(1)	79.81(12)	18.26(6)	0.593(9)
R5.5		451(4)	60.1(2)	78.91(12)	17.96(7)	0.574(11)
R5.6		556(3)	60.1(2)	77.51(9)	17.47(2)	0.609(7)
R5.7		635(3)	60.0(5)	76.74(16)	17.06(1)	0.610(19)
R5.8		684(4)	55.0(3)	72.75(6)	16.78(4)	0.512(16)
Total	*83,900*	*412(3)*	*56.4(3)*	*72.56(11)*	*16.43(3)*	*0.532(11)*
Olivine analyses						
K1	3480	8.1(5)	−0.03(4)	2.41(10)	0.174(21)	−0.006(5)
K2	6150	1.1(4)	0.02(2)	0.34(6)	0.008(8)	−0.002(3)
K3	10,900	1.4(3)	1.96(3)	1.17(3)	0.249(11)	0.007(2)
K4	6450	0.0(4)	1.40(4)	0.75(8)	0.073(24)	0.006(2)
K5	5910	0.8(6)	−0.04(2)	0.31(11)	0.026(22)	−0.005(4)
K6	6470	1.8(3)	0.09(2)	0.17(8)	0.004(19)	−0.006(4)
K7		a.d.	a.d.	a.d.	a.d.	a.d.
A.2.4. RB587B						
Glass analyses (single raster areas)						
spot 0	32,400	635(2)	54.24(22)	77.81(19)	18.20(8)	0.672(6)
R2 a	13,800	8.2(9)	11.81(11)	68.09(24)	14.99(10)	0.465(8)
R3 a	15,300	9.2(6)	13.07(5)	62.17(9)	14.23(8)	0.490(10)
R4 a	15,600	12.2(5)	11.62(7)	63.13(19)	14.52(9)	0.471(11)
R5 a	13,800	11.0(5)	12.67(12)	74.64(11)	17.17(9)	0.584(4)
R6 a	13,800	5.5(8)	11.04(11)	66.72(17)	14.11(9)	0.441(6)
R8 a	20,800	2.6(3)	14.11(7)	68.07(18)	15.17(4)	0.555(6)
R9 a	19,400	15.4(4)	16.76(4)	74.58(10)	17.28(11)	0.657(13)
R10 a	19,800	11.3(3)	16.05(6)	71.89(7)	16.86(4)	0.615(7)
R11 a	17,000	19.1(5)	14.90(11)	75.77(16)	16.90(4)	0.567(7)

Please cite this article in press as: Heber, V.S. et al., Crystal–melt partitioning of noble gases (helium, neon, argon, ..., *Geochim. Cosmochim. Acta* (2007), doi:10.1016/j.gca.2006.11.010

Table A.2 (*continued*)

R12 b	14,700	3.9(3)	11.44(16)	70.92(15)	16.33(5)	0.596(7)
R13 b	14,300	7.6(4)	10.52(9)	76.20(8)	18.31(5)	0.811(16)
Depth profiles in glass						
R1.1		947(5)	62.39(24)	90.28(13)	21.82(9)	0.818(8)
R1.2		1210(4)	52.88(22)	76.11(9)	18.27(5)	0.714(11)
R1.3		1295(5)	45.11(11)	64.20(14)	15.42(2)	0.568(5)
R1.4		1290(16)	37.58(7)	55.96(12)	13.25(7)	0.519(3)
Total	*87,400*	*1185(7)*	*49.49(16)*	*71.64(12)*	*17.19(6)*	*0.655(7)*
R7.1 a		2.7(1.1)	0.97(7)	32.3(2)	7.37(6)	0.191(9)
R7.2 a		6.9(1.0)	4.58(6)	54.0(2)	11.25(7)	0.365(14)
R7.3 a		7.5(1.2)	11.13(15)	86.8(2)	18.85(4)	0.606(6)
R7.4 a		12.1(9)	13.17(22)	85.4(4)	18.81(8)	0.727(14)
R7.5 a		13.1(9)	18.59(22)	77.4(3)	17.16(11)	0.586(14)
R7.6 a		15.9(1.0)	21.09(13)	77.8(2)	17.33(4)	0.610(29)
R7.7 a		17.8(1.3)	24.36(27)	76.5(2)	16.64(9)	0.657(26)
Total	*46,600*	*10.9(1.1)*	*13.41(16)*	*70.0(2)*	*15.34(7)*	*0.534(16)*
Olivine analyses						
K1	4720	5.1(1.5)	0.04(4)	0.70(8)	0.023(13)	0.005(4)
K2	10,200	0.7(5)	0.02(3)	0.23(12)	0.022(4)	0.005(2)
K3	7090	−1.0(9)	0.05(1)	0.13(5)	0.014(5)	−0.003(3)
K4	7414	−1.1(7)	−0.08(4)	0.81(3)	0.098(9)	−0.012(2)
K5	3600	−0.6(1.4)	0.02(4)	0.33(13)	0.055(7)	−0.011(4)
K6	8240	2.0(9)	−0.02(5)	0.18(7)	0.000(6)	0.004(2)
K7	10,200	1.8(8)	0.03(4)	0.02(7)	−0.005(6)	−0.002(2)
K8	6290	8717	447	a.d.	a.d.	201

A.2.5. RB587F

Glass analyses (single raster areas)						
R1	12,200	364(7)	53.5(3)	71.4(4)	19.43(6)	0.737(9)
R2	12,000	415(8)	54.1(3)	72.8(2)	19.12(8)	0.671(17)
R3	11,000	336(11)	55.3(6)	78.2(3)	21.32(6)	0.704(11)
R4	10,600	411(11)	57.6(2)	77.6(3)	19.40(5)	0.746(12)
R6	12,500	351(4)	55.6(3)	73.2(2)	20.14(8)	0.766(14)
R7	9410	343(4)	56.8(2)	78.4(3)	20.81(15)	0.632(9)
R9 a	10,600	7.5(8)	23.3(1)	71.2(1)	19.86(7)	0.648(12)
R10 a	10,200	2.6(7)	19.1(1)	71.7(1)	19.81(2)	0.826(9)
Depth profile in glass						
R5.1		64(4)	19.7(1)	28.2(3)	6.96(5)	0.211(9)
R5.2		172(6)	41.0(1)	48.2(1)	11.98(6)	0.407(9)
R5.3		371(6)	61.9(6)	78.5(4)	20.52(10)	0.655(6)
R5.4		464(6)	65.6(3)	88.0(2)	22.84(5)	0.710(14)
R5.5		585(7)	63.4(3)	83.7(4)	22.73(13)	0.575(24)
R5.6		695(8)	65.1(2)	82.2(2)	21.58(7)	0.789(8)
R5.7		773(6)	59.9(5)	77.9(3)	20.61(4)	0.894(13)
Total	*45,800*	*446(6)*	*53.8(3)*	*69.5(3)*	*18.17(7)*	*0.606(12)*
Olivine analyses						
k1	3060	2.2(2.6)	0.16(9)	2.33(19)	0.473(6)	−0.010(3)
k2	1380	3.1(2.9)	−1.06(11)	0.38(22)	0.020(13)	0.019(13)
k3	3470	17.7(1.7)	0.63(4)	3.24(12)	0.712(21)	0.005(5)
k4	3440	9.4(1.5)	0.09(3)	0.63(13)	0.021(5)	0.018(5)
k5	6100	417(1)	20.7(2)	176.1(5)	96.0(2)	9.52(3)
k6	3410	1.9(2.0)	0.01(8)	1.94(15)	0.441(17)	−0.007(9)
k7	1150	−11.3(4.1)	0.28(6)	2.74(74)	0.771(55)	0.030(30)
k8	2240	8.0(2.2)	0.18(8)	1.62(19)	0.501(46)	0.017(10)
k9	3590	−2.9(1.7)	0.02(7)	0.00(12)	0.023(13)	−0.003(3)
k10	1210	14.6(3.3)	0.10(19)	1.08(47)	−0.030(7)	−0.007(7)

A.2.6. RB586A

Glass analyses (single raster areas)						
R1	6590	—[a]	138.7(6)	190.0(5)	37.47(5)	0.664(4)
R2	7520	—	136.4(4)	187.4(7)	35.23(12)	0.585(11)
R3	12,000	—	131.4(5)	184.5(4)	33.16(7)	0.702(4)
R4	12,000	—	135.9(4)	191.7(4)	35.54(17)	0.741(22)

(*continued on next page*)

Table A.2 (*continued*)

Analyses	Ablated volume (μm^3)	^{4}He	^{22}Ne	^{40}Ar	^{84}Kr	^{132}Xe
R5	12,000	21(4)	132.3(7)	195.0(3)	32.44(6)	1.244(14)
R6	11,900	29(5)	127.1(5)	181.7(1)	30.45(6)	0.981(9)
R7	11,400	17(5)	132.5(2)	181.7(1)	39.92(4)	1.262(8)
R9	11,600	27(4)	142.0(5)	201.6(1)	34.83(6)	2.030(38)
R10 a	14,500	2.0(5)	58.7(2)	166.9(3)	31.90(12)	0.702(15)
R11 a	12,200	−0.3(6)	62.6(1)	189.3(2)	34.72(5)	1.007(9)
R12 a	12,900	1.4(7)	74.8(3)	181.2(2)	39.25(9)	1.067(12)
Depth profile in glass						
R8.1		25(4)	75.6(2)	107.3(5)	21.85(3)	0.697(15)
R8.2		20(4)	81.9(3)	114.1(3)	23.10(7)	0.716(9)
R8.3		14(4)	109.9(3)	151.3(4)	30.96(6)	0.835(6)
R8.4		31(4)	141.2(4)	191.2(2)	40.06(14)	1.052(17)
R8.5		16(4)	153.7(5)	211.2(6)	43.77(16)	1.266(35)
R8.6		15(7)	138.6(3)	196.1(6)	41.32(16)	1.057(24)
R8.7		13(4)	136.9(3)	189.5(5)	39.61(7)	1.055(8)
R8.8		11(4)	132.1(6)	186.4(3)	38.93(15)	1.082(9)
Total	*57,600*	*18(5)*	*121.2(4)*	*168.4(4)*	*34.95(11)*	*0.970(16)*
Clinopyroxene analyses						
K1	10,800	0.2(6)	0.07(2)	0.15(4)	0.021(5)	0.016(3)
K2	6960	1.9(1.1)	0.09(3)	−0.07(5)	−0.001(5)	−0.002(2)
K3	8460	−1.4(6)	0.07(3)	0.39(6)	0.021(4)	0.001(2)
K4	3990	2.3(1.0)	0.03(8)	−0.16(11)	0.002(2)	0.002(2)
K5	12,700	21.8(4)	0.42(3)	7.07(6)	1.292(8)	0.037(3)
K6	13,600	0.9(3)	0.02(3)	0.90(5)	0.184(3)	0.0032(6)
K7	8638	2.1(4)	0.05(4)	0.97(5)	0.162(9)	0.0010(10)
K8	6226	0.5(5)	0.11(2)	0.20(7)	0.015(1)	−0.003(0)
K9	10,700	3.9(4)	0.05(1)	6.32(4)	1.129(15)	0.079(2)
K10	11,500	−0.9(5)	−0.01(2)	0.24(5)	0.006(3)	0

Gas concentrations are given in 10^{-4} cm^3 STP/g. Numbers in parentheses represent 1 − σ uncertainties in units of the least significant digit.
a.d. above mass spectrometer range of detection.
a, Measurement after first heating; b, after second heating.
[a] Helium is not given for R1–R4 due to instable He sensitivity conditions in the mass spectrometer.

the range of literature data reported for basaltic glasses and extrapolated to 23 °C, e.g., 1×10^{-15} cm^2/s (Trull, 1989) and $\sim 3 \times 10^{-13}$ cm^2/s (Jambon and Shelby, 1980). (Note that sample RB588C was not further considered in this work because of missing calibration and only suboptimal ablation conditions. Therefore, the data in Table A.1 and in Fig. A.1 are given in Volt/g.) In contrast, Ne and Ar abundances at same depth levels show that noble gases heavier than He are not affected by diffusive loss. The slight decrease of the Ne abundance with increasing depth in Fig. A.1 is due to a continuous decrease of the ablatable area within the pit with increasing depth that is not accounted for here.

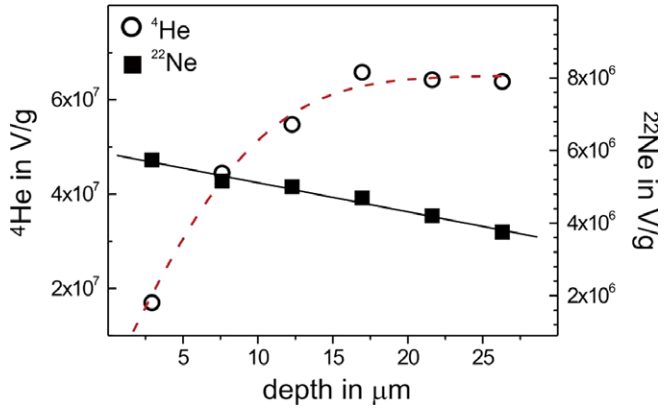

Fig. A.1. Depth profiles of He (circles, left ordinate) and Ne (squares, right ordinate) concentration in the N2SFo glass (RB588C). Helium clearly diffused out of the uppermost ~15 μm of the glass during 153 days storage at room temperature. This loss was fitted by the error function (dashed line) as described above, resulting in a He diffusion coefficient for N2SFo glasses at 23 °C of 2.4×10^{-14} cm^2/s. In contrast, Neon concentrations are constant with depth, (linear fit, solid line), suggesting no diffusive loss of Ne at these storage conditions. The slight decrease of the Ne data with depth is due to a continuous decrease of the ablatable area, i.e., the extracted volume, with increasing depth.

In order to calculate the original He concentration in the glass, we corrected for the loss that occurred between sample cutting and polishing and the sample analysis date (up to one year). Up to 90% of the He is lost from the uppermost 5 μm (the mean depth of the raster pits ablated in the glasses of RB586, RB587, RB588, RB589). The original He concentration for all glasses was therefore calculated using their measured Ne concentrations and the ^{4}He/^{22}Ne ratio obtained from analyses well below the surface in samples polished shortly before analysis. For the N2SFo glasses a ^{4}He/^{22}Ne ratio of 60.0 and for the $Di_{60}Ab_{40}$ glasses of 31.6 was obtained by the analysis of RB587F and RB586AII, respectively. Depth profiles in all glasses showed that Ne is quantitatively retained (see Fig. A.1 as one example).

Please cite this article in press as: Heber, V.S. et al., Crystal–melt partitioning of noble gases (helium, neon, argon, ..., *Geochim. Cosmochim. Acta* (2007), doi:10.1016/j.gca.2006.11.010

References

Albarède, F., 1998. Time-dependent models of U–Th–He and K–Ar evolution and the layering of mantle convection. *Chem. Geol.* **145**, 413–429.

Allan, N.L., Du, Z., Lavrentiev, M.Y., Blundy, J.D., Purton, J.A., van Westrenen, W., 2003. Atomistic simulation of mineral–melt trace-element partitioning. *Phys. Earth Planet. Interiors* **139**, 93–111.

Allègre, C., Hamelin, B., Provost, A., Dupre, B., 1987. Topology in isotopic multispace and origin of mantle chemical heterogeneities. *Earth Planet. Sci. Lett.* **81**, 319–337.

Allègre, C., Moreira, M., 2004. Rare gas systematics and the origin of oceanic islands: the key role of entrainment at the 670 km boundary layer. *Earth Planet. Sci. Lett.* **228**, 85–92.

Ballentine, C.J., van Keken, P.E., Porcelli, D., Hauri, E.H., 2002. Numerical models, geochemistry and the zero-paradox noble gas mantle. *Philos. Trans. R. Soc. Lond. A* **360**, 2611–2631.

Ballentine, C.J., van Keken, P.E., Porcelli, D., Hauri, E.H., 2003. Noble gases and changing models of mantle evolution. *Geophys. Res. Abstr.* **5**, 14588.

Beattie, P., 1993. The generation of uranium series disequilibria by partial melting of spinel peridotite: constraints from partitioning studies. *Earth Planet. Sci. Lett.* **117** (3–4), 379–391.

Bijwaard, H., Spakman, W., 1998. Closing gap between regional and global travel time tomography. *J. Geophys. Res.* **103** (B12), 30055–30078.

Blundy, J., Wood, B., 1994. Prediction of crystal–melt partition coefficients from elastic moduli. *Nature* **372**, 452–454.

Broadhurst, C.L., Drake, M.J., Hagee, B.E., Bernatowicz, T.J., 1990. Solubility and partitioning of Ar in anorthite, diopside, forsterite, spinel, and synthetic basaltic liquids. *Geochim. Cosmochim. Acta* **54**, 299–309.

Broadhurst, C.L., Drake, M.J., Hagee, B.E., Bernatowicz, T.J., 1992. Solubility and partitioning of Ne, Ar, Kr and Xe in minerals and synthetic basaltic melts. *Geochim. Cosmochim. Acta* **56**, 709–723.

Brooker, R.A., Du, Z., Blundy, J., Kelley, S.P., Allan, N.L., Wood, B., Chamorro, E.M., Wartho, J.-A., Purton, J.A., 2003a. The 'zero charge' partitioning behaviour of noble gases during mantle melting. *Nature* **423**, 738–741.

Brooker, R.A., Heber, V.S., Kelley, S.P., Wood, B., 2003b. Noble gas partitioning behaviour during mantle melting: a possible explanation for 'The He paradox'? *EOS Trans. AGU, Fall meet. Suppl.*

Brooker, R.A., Wartho, J.-A., Carroll, M.R., Kelley, S.P., Draper, D.S., 1998. Preliminary UVLAMP determinations of argon partition coefficient for olivine and clinopyroxene grown from silicate melts. *Chem. Geol.* **147**, 185–200.

Carroll, M.R., Draper, D.S., 1994. Noble gases as trace elements in magmatic processes. *Chem. Geol.* **117**, 37–56.

Carroll, M.R., Draper, D.S., Brooker, R.A., Kelley, S.P., 1994. Noble gas solubilities in melt and crystals. In: Matsuda, J. (Ed.), *Noble Gas Geochemistry and Cosmochemistry*. Terra Scientific Publishing Company, pp. 325–341.

Carroll, M.R., Stolper, E.M., 1993. Noble gas solubilities in silicate melts and glasses—new experimental results for argon and the relationship between solubility and ionic porosity. *Geochim. Cosmochim. Acta* **57** (23–24), 5039–5051.

Chamorro, E.M., Brooker, R.A., Wartho, J.-A., Wood, B.J., Kelley, S.P., Blundy, J.D., 2002. Ar and K partitioning between clinopyroxene and silicate melt to 8 GPa. *Geochim. Cosmochim. Acta* **66** (3), 507–519.

Class, C., Goldstein, S.L., 2005. Evolution of helium isotopes in the Earth's mantle. *Nature* **436**, 1107–1112.

Deer, W.A., Howie, R.A., Zussmann, J., 1992. *An Introduction to the Rock-Forming Minerals*. Longman, London.

Dingwell, D.B., Hess, K.U., Romano, C., 1998. Extreme fluid behaviour of hydrous peralkaline rhyolites. *Earth Planet. Sci. Lett.* **158**, 31–38.

Donaldson, C.H., 1975. An experimental investigation of olivine morphology. *Contrib. Mineral. Petrol.* **57**, 187–213.

Farley, K.A., Neroda, E., 1998. Noble gases in the Earth's mantle. *Annu. Rev. Earth Planet. Sci.* **26**, 189–218.

Fukao, Y., Widiyantoro, S., Obayashi, M., 2001. Stagnant slabs in the upper and lower mantle transition region. *Rev. Geophys.* **39** (3), 291–323.

Gale, J.D., 1997. GULP: A computer program for the symmetry-adapted simulation of solids. *J. Chem. Soc. Faraday Trans.* **93**, 629–637.

Graham, D., 2002. Noble gas isotope geochemistry of MORBs and OIBs. In: Porcelli, D., Ballentine, C.J., Wieler, R. (Eds.), *Noble Gases in Geochemistry and Cosmochemistry*. *Rev. Min. Geochem.*, vol. 46, pp. 247–317.

Graham, D., Lupton, J., Albarède, F., Condomines, M., 1990. Extreme temporal homogeneity of helium isotopes at Piton de la Fournaise, Reunion Island. *Nature* **347**, 545–548.

Hart, S.R., Brooks, C., 1974. Clinopyroxene-matrix partitioning of K, Rb, Cs, Sr and Ba. *Geochim. Cosmochim. Acta* **38** (12), 1799–1806.

Hazelton, G.B., Axen, G., Lovera, O., 2003. Argon retention properties of silicate glasses and implications for 40Ar/39Ar age and noble gas diffusion. *Contrib. Mineral. Petrol.* **145**, 1–14.

Heber, V.S., 2002. Ancient solar wind noble gases in lunar and meteoritic archives and tests for modern solar wind collection with the GENESIS mission. PhD Thesis. ETH Zürich, Switzerland.

Heber, V.S., Brooker, R.A., Kelley, S.P., Wood, B.J., 2004. Diffusion behaviour of noble gases in mantle minerals: high resolution UV laser depth profiling. In: *10th Symposium on Experimental Mineralogy, Petrology and Geochemistry*, Lithos 73, S49.

Hiyagon, H., Ozima, M., 1986. Partitioning of noble gases between olivine and basalt melt. *Geochim. Cosmochim. Acta* **50**, 2045–2057.

Hofmann, A.W., 1997. Mantle geochemistry: the message from oceanic volcanism. *Nature* **385**, 219–229.

Jambon, A., Shelby, J.E., 1980. Helium diffusion and solubility in obsidians and basaltic glass in the range 200–300 °C. *Earth Planet. Sci. Lett.* **51**, 206–214.

Jambon, A., Weber, H.W., Braun, O., 1986. Solubility of He, Ne, Ar, Kr, and Xe in a basalt melt in the range 1250–1600 °C. Geochemical implications. *Geochim. Cosmochim. Acta* **50**, 401–408.

Kamijo, K., Hashizume, K., Matsuda, J., 1998. Noble gas constraints on the evolution of the atmosphere-mantle system. *Geochim. Cosmochim. Acta* **62** (13), 2311–2321.

Kaneoka, I., 1983. Noble gas constraints on the layered structure of the mantle. *Nature* **302**, 698–700.

Kelley, S.P., Arnaud, N.O., Turner, S.P., 1994. High spatial resolution 40Ar/39Ar investigations using an ultra-violet laser probe extraction technique. *Geochim. Cosmochim. Acta* **58** (16), 3519–3525.

Kurz, M.D., Jenkins, W.J., Schilling, J.G., Hart, S.R., 1982. Helium isotopic variations in the mantle beneath the central North Atlantic Ocean. *Earth Planet. Sci. Lett.* **58**, 1–14.

Lange, R.M., Carmichael, I.S.E., 1987. Densities of Na_2O–K_2O–CaO–MgO–FeO–Fe_2O_3–Al_2O_3–TiO_2–SiO_2 liquids: new measurements and derived partial molar properties. *Geochim. Cosmochim. Acta* **51**, 1549–1560.

Lux, G., 1987. The behaviour of noble gases in silicate liquids: solution, diffusion, bubbles and surface effects, with applications to natural samples. *Geochim. Cosmochim. Acta* **51**, 1549–1560.

Marty, B., Lussiez, P., 1993. Constraints on rare gas partitioning coefficients from analysis of olivine-glass from a picritic mid-oceanic ridge basalt. *Chem. Geol.* **106**, 1–7.

Meibom, A., Anderson, D.L., Sleep, N.H.R.F., Chamberlain, C.P., Hren, M.T., Wooden, J.L., 2003. Are high He-3/He-4 ratios in oceanic basalts an indicator of deep-mantle plume components? *Earth Planet. Sci. Lett.* **208** (3–4), 197–204.

Miyazaki, A., Hiyagon, H., Sugiura, N., Hirose, K., Takahashi, E., 2004. Solubilities of nitrogen and noble gases in silicate melts under various oxygen fugacities: implications for the origin and degassing history of nitrogen and noble gases in the Earth. *Geochim. Cosmochim. Acta* **68** (2), 387–401.

Please cite this article in press as: Heber, V.S. et al., Crystal–melt partitioning of noble gases (helium, neon, argon, ..., *Geochim. Cosmochim. Acta* (2007), doi:10.1016/j.gca.2006.11.010

Nakamura, A., Schmalzried, H., 1983. On the nonstoichiometry and point-defects of olivine. *Phys. Chem. Miner.* **10**, 27–37.

Nowak, M., Schreen, D., Spickenbom, K., 2004. Argon and CO_2 on the race track in silicate melts: a tool for the development of a CO_2 speciation and diffusion model. *Geochim. Cosmochim. Acta* **68** (24), 5127–5138.

O'Nions, R.K., 1987. Relationships between chemical and convective layering in the Earth. *J. Geol. Soc. Lond.* **144**, 259–274.

Ozima, M., Igarashi, G., 2000. The primordial noble gases in the Earth: a key constraint on Earth evolution models. *Earth Planet. Sci. Lett.* **176**, 219–232.

Ozima, M., Podosek, F.A., 2002. *Noble Gas Geochemistry*. Cambridge University Press, Cambridge.

Parman, S.W., Kurz, M.D., Hart, S.R., Grove, T.L., 2005. Helium solubility in olivine and implications for high 3He/4He in ocean island basalts. *Nature* **437**, 1140–1143.

Porcelli, D., Wasserburg, G.J., 1995. Mass transfer of helium, neon, argon, and xenon through a steady-state upper mantle. *Geochim. Cosmochim. Acta* **59** (23), 4921–4937.

Porcelli, D., Woolum, D., Cassen, P., 2001. Deep Earth rare gases: initial inventories, capture from the solar nebula, and losses during Moon formation. *Earth Planet. Sci. Lett.* **193** (1–2), 237–251.

Roberts, H.J., 1999. An investigation of a polymetamorphic terrain using ^{40}Ar–^{39}Ar geochronology. PhD Thesis. The Open University, Milton Keynes, UK.

Roselieb, K., Blanc, P., Büttner, H., Jambon, A., Rammensee, W., Rosenhauer, M., Vielzeuf, D., Walter, H., 1997. Experimental study of argon sorption in quartz: evidence for argon solubility. *Geochim. Cosmochim. Acta* **61**, 533–542.

Schmidt, B.C., Keppler, H., 2002. Experimental evidence for high noble gas solubilities in silicate melts under mantle pressures. *Earth Planet. Sci. Lett.* **195**, 277–290.

Shibata, T., Takahashi, E., Ozima, M., 1994. Noble gas partition between basaltic melt and olivine crystals at high pressures. In: Matsuda, J. (Ed.), *Noble Gas Geochemistry and Cosmochemistry*. Terrapub, pp. 343–354.

Smyth, D.M., Stocker, R.L., 1975. Point defects and nonstoichiometry in forsterite. *Phys. Earth Planet. Int.* **10**, 183–192.

Trull, T.W., 1989. Diffusion of helium isotopes in silicate glasses and minerals; implications for petrogenesis and geochronology. Thesis, PhD Thesis. MIT, Cambridge, MA, USA.

Trull, T.W., Kurz, M.D., 1993. Experimental measurements of 3He and 4He mobility in olivine and clinopyroxene at magmatic temperatures. *Geochim. Cosmochim. Acta* **57**, 1313–1324.

Valbracht, P.J., Honda, M., Staudigel, H., McDougall, I., Trost, A.P., 1994. Noble gas partitioning in natural samples: results from coexisting glass and olivine phenocrysts in four Hawaiian submarine basalts. In: Matsuda, J. (Ed.), *Noble Gas Geochemistry and Cosmochemistry*. Terrapub, pp. 373–381.

van der Hilst, R.D., Widiyantoro, S., Engdahl, E.R., 1997. Evidence for deep mantle circulation from global tomography. *Nature* **386**, 578–585.

van Keken, P.E., Ballentine, C.J., 1999. Dynamical models of mantle volatile evolution and the role of phase transitions and temperature-dependent rheology. *J. Geophys. Res.* **104** (B4), 7137–7151.

van Keken, P.E., Hauri, E.H., Ballentine, C.J., 2002. Mantle mixing: the generation, preservation and destruction of chemical heterogeneity. *Annu. Rev. Earth Planet. Sci.* **30**, 493–525.

Wartho, J.-A., Kelley, S.P., Brooker, R.A., Carroll, M.R., Villa, I.M., Lee, R.L., 1999. Direct measurement of Ar diffusion profiles in a gem-quality Madagascar K-feldspar using the ultra-violet laser ablation microprobe (UVLAMP). *Earth Planet. Sci. Lett.* **170**, 141–153.

Watson, E.B., Cherniak, D.J., 2003. Lattice diffusion of Ar in quartz, with constraints on Ar solubility and evidence of nanopores. *Geochim. Cosmochim. Acta* **67** (11), 2043–2062.

Wood, B.J., Blundy, J.D., 2001. The effect of cation charge on crystal–melt partitioning of trace elements. *Earth Planet. Sci. Lett.* **188** (1–2), 59–71.

Wood, B.J., Blundy, J.D., Robinson, J.A.C., 1999. The role of clinopyroxene in generating U-series disequilibrium during mantle melting. *Geochim. Cosmochim. Acta* **63** (10), 1613–1620.

Zhang, Y., Xu, Z., 1995. Atomic radii of noble gas elements in condensed phases. *Am. Mineral.* **80**, 670–675.

Please cite this article in press as: Heber, V.S. et al., Crystal–melt partitioning of noble gases (helium, neon, argon, ..., *Geochim. Cosmochim. Acta* (2007), doi:10.1016/j.gca.2006.11.010